Mon. Not. R. Astron. Soc. **367,** 113–131 (2006) doi:10.1111/j.1365-2966.2005.09953.x

Detecting shock waves in cosmological smoothed particle hydrodynamics simulations

C. Pfrommer,[1,2⋆] V. Springel,[1⋆] T. A. Enßlin[1⋆] and M. Jubelgas[1⋆]

[1]*Max-Planck-Institut für Astrophysik, Karl-Schwarzschild-Straße 1, Postfach 1317, 85741 Garching, Germany*
[2]*Canadian Institute for Theoretical Astrophysics, University of Toronto, 60 St. George Street, Toronto, Ontario, Canada M5S 3H8*

Accepted 2005 December 5. Received 2005 December 2; in original form 2005 September 8

ABSTRACT

We develop a formalism for the identification and accurate estimation of the strength of structure formation shocks *during* cosmological smoothed particle hydrodynamics simulations. Shocks play a decisive role not only for the thermalization of gas in virializing structures but also for the acceleration of relativistic cosmic rays (CRs) through diffusive shock acceleration. Our formalism is applicable both to ordinary non-relativistic thermal gas, and to plasmas composed of CRs and thermal gas. To this end, we derive an analytic solution to the one-dimensional Riemann shock tube problem for a composite plasma of CRs and thermal gas. We apply our methods to study the properties of structure formation shocks in high-resolution hydrodynamic simulations of the Lambda cold dark matter (ΛCDM) model. We find that most of the energy is dissipated in weak internal shocks with Mach numbers $\mathcal{M} \sim 2$ which are predominantly central flow shocks or merger shock waves traversing halo centres. Collapsed cosmological structures are surrounded by external shocks with much higher Mach numbers up to $\mathcal{M} \sim 1000$, but they play only a minor role in the energy balance of thermalization. This is because of the higher pre-shock gas densities within non-linear structures, and the significant increase of the mean shock speed as the characteristic halo mass grows with cosmic time. We show that after the epoch of cosmic reionization the Mach number distribution is significantly modified by an efficient suppression of strong external shock waves due to the associated increase of the sound speed of the diffuse gas. Invoking a model for CR acceleration in shock waves, we find that the average strength of shock waves responsible for CR energy injection is higher than that for shocks that dominate the thermalization of the gas. This implies that the dynamical importance of shock-injected CRs is comparatively large in the low-density, peripheral halo infalling regions, but is less important for the weaker flow shocks occurring in central high-density regions of haloes. When combined with radiative dissipation and star formation, our formalism can also be used to study CR injection by supernova shocks, or to construct models for shock-induced star formation in the interstellar medium.

Key words: shock waves – methods: numerical – cosmic rays – galaxies: clusters: general – intergalactic medium – large-scale structure of Universe.

1 INTRODUCTION

1.1 Structure formation shock waves

Cosmological shock waves form abundantly in the course of structure formation, both due to infalling pristine cosmic plasma which accretes on to filaments, sheets and haloes, as well as due to supersonic flows associated with merging substructures (Quilis, Ibanez & Saez 1998; Miniati et al. 2000; Gabici & Blasi 2003; Ryu et al. 2003; Pavlidou & Fields 2005). Additionally, shock waves occur due to non-gravitational physics in the interstellar and intracluster media, e.g. as a result of supernova explosions. Structure formation shock waves propagate through the cosmic tenuous plasma, which is compressed at the transition layer of the shock while a part of the kinetic energy of the incoming plasma is dissipated into internal energy of the post-shock gas. Because of the large collisional mean free path, the energy transfer proceeds through collective electromagnetic viscosity which is provided by ubiquitous magnetic irregularities (Wentzel 1974; Kennel, Edmiston & Hada 1985).

⋆E-mail: pfrommer@cita.utoronto.ca (CP); volker@mpa-garching.mpg.de (VS); ensslin@mpa-garching.mpg.de (TAE); jubelgas@mpa-garching.mpg.de (MJ)

Cosmologically, shocks are important in several respects. (1) Shock waves dissipate gravitational energy associated with hierarchical clustering into thermal energy of the gas contained in dark matter haloes, thus supplying the intrahalo medium with entropy and thermal pressure support. Radiative cooling is then required to compress the gas further to densities that will allow star formation. (2) Shocks also occur around moderately overdense filaments, which leads to a heating of the intragalactic medium. Sheets and filaments are predicted to host a warm–hot intergalactic medium with temperatures in the range $10^5 < T < 10^7$ K whose evolution is primarily driven by shock heating from gravitational perturbations breaking on mildly non-linear, non-equilibrium structures (Hellsten, Gnedin & Miralda-Escudé 1998; Cen & Ostriker 1999; Davé et al. 2001; Furlanetto & Loeb 2004; Kang et al. 2005). Thus, the shock-dissipated energy traces the large-scale structure and contains information about its dynamical history. (3) Besides thermalization, collisionless shocks are also able to accelerate ions of the high-energy tail of the Maxwellian through diffusive shock acceleration (DSA) (for reviews see Drury 1983; Blandford & Eichler 1987; Malkov & O'C Drury 2001). These energetic ions are reflected at magnetic irregularities through magnetic resonances between the gyro motion and waves in the magnetized plasma and are able to gain energy in moving back and forth through the shock front. This acceleration process typically yields a cosmic ray (CR) population with a power-law distribution of the particle momenta. Non-linear studies of DSA have shown that a considerable part of the kinetic energy flux passing through shocks can be channelled into non-thermal populations, up to about one-half of the initial kinetic energy of the shock (Berezhko, Ksenofontov & Yelshin 1995; Ellison, Baring & Jones 1996; Malkov 1998, 1999; Kang, Jones & Gieseler 2002). Note that CRs have sufficient momentum not to resonate with the electromagnetic turbulence in the shock front itself. They hence experience the shock as a discontinuity, i.e. the CR population is adiabatically compressed by the shock (e.g. Drury 1983).

Indeed, CR electrons have been observed in the intracluster medium (ICM) of galaxy clusters through their diffuse synchrotron emission (Kim et al. 1989; Giovannini et al. 1993; Deiss et al. 1997). In addition to these extended radio haloes which show a similar morphology compared to the thermal X-ray emission, there have been extended radio relics observed in the cluster periphery (e.g. Röttgering et al. 1997) which might well coincide with merger shock waves as proposed by Enßlin et al. (1998). Some clusters have also been reported to exhibit an excess of hard X-ray emission compared to the expected thermal bremsstrahlung of the hot ICM, most probably produced by inverse Compton upscattering of cosmic microwave background photons by relativistic electrons (Fusco-Femiano et al. 1999; Sanders, Fabian & Dunn 2005). It has been proposed that a fraction of the diffuse cosmological γ-ray background radiation originates from the same processes (Loeb & Waxman 2000; Miniati 2002; Berrington & Dermer 2003; Reimer et al. 2003; Kuo, Bowyer & Hwang 2005).

To date, there are two different scenarios explaining these non-thermal emission processes. (1) Re-acceleration processes of 'mildly' relativistic electrons ($\gamma \simeq 100$–300) being injected over cosmological time-scales into the ICM by sources like radio galaxies, supernova remnants, merger shocks or galactic winds, which all can provide an efficient supply of highly energetic CR electrons. Owing to their long lifetimes of the order of 10^9 yr these 'mildly' relativistic electrons can accumulate within the ICM (Sarazin 2002), until they experience continuous *in situ* acceleration either via shock acceleration or resonant pitch angle scattering on turbulent Alfvén waves (Jaffe 1977; Schlickeiser, Sievers & Thiemann 1987; Brunetti et al. 2001; Ohno, Takizawa & Shibata 2002; Brunetti et al. 2004). (2) In the ICM, the CR protons have lifetimes of the order of the Hubble time (Völk, Aharonian & Breitschwerdt 1996), which is long enough to diffuse away from the production site and to maintain a space-filling distribution over the cluster volume. These CR protons can interact hadronically with the thermal ambient gas producing secondary electrons, neutrinos and γ-rays in inelastic collisions throughout the cluster volume, generating radio haloes through synchrotron emission (Dennison 1980; Vestrand 1982; Blasi & Colafrancesco 1999; Dolag & Enßlin 2000; Pfrommer & Enßlin 2003, 2004a,b). Cosmological simulations support the possibility of a hadronic origin of cluster radio haloes (Miniati et al. 2001).

1.2 Hydrodynamical simulations

Hydrodynamical solvers of cosmological codes are generally classified into two main categories: (1) Lagrangian methods like smoothed particle hydrodynamics (SPH) which discretize the mass of the fluid and (2) Eulerian codes, which discretize the fluid volume. SPH methods were first proposed by Gingold & Monaghan (1977) and Lucy (1977) and approximate continuous fluid quantities by means of kernel interpolation over a set of tracer particles. Over the years, SPH techniques have been steadily improved and found widespread applications in cosmological problems (Evrard 1988; Hernquist & Katz 1989; Navarro & White 1993; Springel & Hernquist 2002).

In contrast, Eulerian methods discretize space and represent continuous fields on a mesh. Originally, Eulerian codes employed a mesh which is fixed in space (Cen & Ostriker 1993; Yepes et al. 1995) or adaptively moving (Pen 1998), while more recently, adaptive mesh refinement (AMR) algorithms have been developed for cosmological applications (Berger & Colella 1989; Bryan & Norman 1997; Norman & Bryan 1999; Abel, Bryan & Norman 2002; Kravtsov, Klypin & Hoffman 2002; Refregier & Teyssier 2002), which can adapt to regions of interest in a flexible way.

Grid-based techniques offer superior capabilities for capturing hydrodynamical shocks. In some algorithms, this can be done even without the aid of artificial viscosity, thanks to the use of Riemann solvers at the cell level, so that a very low residual numerical viscosity is achieved. However, codes employing static meshes still lack the resolution and flexibility necessary to tackle structure formation problems in a hierarchically clustering universe, which is characterized by a very large dynamic range and a hierarchy of substructure at all stages of the evolution. For example, techniques based on a fixed mesh are seriously limited when one tries to study the formation of individual galaxies in a cosmological volume, simply because the internal galactic structure such as disc and bulge components can then in general not be sufficiently well resolved. A new generation of AMR codes which begin to be applied in cosmology may in principle resolve this problem. However, a number of grid-based problems remain even here, for example the dynamics is not Galilean invariant, and there can be spurious advection and mixing errors, especially for large bulk velocities across the mesh.

These problems can be avoided in SPH thanks to its Lagrangian nature, and its accurate treatment of self-gravity is particularly well suited for structure formation problems. SPH adaptively and automatically increases the resolution in dense regions such as galactic haloes or centres of galaxy clusters, which are the regions of primary interest in cosmology. One drawback of SPH is the dependence on the artificial viscosity which has to deliver the necessary entropy

injection in shocks. While the parametrization of the artificial viscosity can be motivated in analogy with the Riemann problem (Monaghan 1997), the shocks themselves are broadened over the SPH smoothing scale and not resolved as discontinuities, but post-shock quantities are calculated very accurately. However, to date it has not been possible to identify and measure the shock strengths instantaneously with an SPH simulation.

Being interested in dynamical implications of CRs on structure formation and galaxy evolution, one faces not only the problem of the interplay of gravity and hydrodynamics of a plasma composed of CRs and thermal particles but in addition radiative processes such as cooling and supernova feedback. To date, AMR codes have not yet matured to the point that they can address all these requirements throughout a cosmological volume, although there are recent efforts along these lines (e.g. Jones & Kang 2005; Kang & Jones 2005). It would therefore be ideal if SPH codes for structure formation could acquire the ability to detect shocks reliably *during* simulations. Previous work on shock detection in SPH simulations (Keshet et al. 2003) was restricted to a posteriori analysis of two subsequent simulation time-slices, which can then be used to approximately detect a certain range of shocks as entropy jumps.

1.3 Motivation and structure

This article seeks to close this gap in order to allow studies of the following questions. (1) The cosmic evolution of shock strengths provides rich information about the thermal history of the baryonic component of the Universe: where and when is the gas heated to its present temperatures, and which shocks are mainly responsible for it? Does the missing baryonic component in the present-day universe reside in a warm–hot intergalactic medium? (2) CRs are accelerated at structure formation shocks through DSA: what are the cosmological implications of such a CR component? (3) Shock waves are modified by non-linear back-reaction of the accelerated CRs and their spatial diffusion into the pre-shock regime: does this change the cosmic thermal history or give rise to other effects? (4) Simulating realistic CR profiles within galaxy clusters can provide detailed predictions for the expected radio synchrotron and γ-ray emission: what are the observational signatures of this radiation that is predicted to be observed with the upcoming new generation of γ-ray instruments (imaging atmospheric Čerenkov telescopes and the GLAST[1] satellite) and radio telescopes (LOFAR[2] and extended Very Large Array)?

The purpose of this paper is to study the properties of structure formation shock waves in cosmological simulations, allowing us to explore their role for the thermalization of the pristine plasma, as well as for the acceleration of relativistic CRs through DSA. In particular, we develop a framework for quantifying the importance of CRs during cosmological structure formation, including an accounting of the effects of adiabatic compressions and rarefactions of CR populations, as well as of numerous non-adiabatic processes. Besides CR injection by structure formation shocks, the latter include CR shock injection of supernova remnants, *in situ* re-acceleration of CRs, spatial diffusion of CRs, CR energy losses due to Coulomb interactions, bremsstrahlung, hadronic interactions with the background gas and the associated γ-ray and radio emission due to subsequent pion decay. A full description of these CR processes and their formulation for cosmological applications is described in Enßlin et al. (in preparation), while the numerical implementation within the SPH formalism is given by Jubelgas et al. (in preparation). In this work we provide a crucial input for this modelling: a formalism for identifying and accurately estimating the strength of structure formation shocks on-the-fly during cosmological SPH simulations.

The paper is structured as follows. The basic CR variables are introduced in Section 2. The formalism for identifying and measuring the Mach number of shock waves instantaneously within an SPH simulation is described in Section 3 for a purely thermal gas as well as for a composite plasma of CRs and thermal gas. The numerical implementation of the algorithm is discussed in Section 4. In Section 5, we compare shock tube simulations to analytic solutions of the Riemann problem which are presented in Appendices A and B. Finally, in Section 6, we perform cosmological non-radiative simulations to study CR energy injection at shocks, and the influence of reionization on the Mach number distribution. A summary in Section 7 concludes the paper.

2 BASIC COSMIC RAY VARIABLES

Since we only consider CR protons,[3] which are at least in our Galaxy the dominant CR species, it is convenient to introduce the dimensionless momentum $p = P_\mathrm{p}/(m_\mathrm{p} c_\mathrm{light})$. CR electrons with $\gamma < 100$ experience efficient Coulomb losses such that their energy density is significantly diminished compared to the CR energy density (Sarazin 2002). The differential particle momentum spectrum per volume element is assumed to be a single power law above the minimum momentum q:

$$f(p) = \frac{\mathrm{d}N}{\mathrm{d}p\,\mathrm{d}V} = C\, p^{-\alpha}\, \theta(p-q). \tag{2.1}$$

$\theta(x)$ denotes the Heaviside step function. Note that we use an effective one-dimensional distribution function $f(p) \equiv 4\pi p^2 f^{(3)}(p)$. The CR population can hydrodynamically be described by an isotropic pressure component as long as the CRs are coupled to the thermal gas by small-scale chaotic magnetic fields. The differential CR spectrum can vary spatially and temporally (although for brevity we suppress this in our notation) through the spatial dependence of the normalization $C = C(\boldsymbol{r}, t)$ and the cut-off $q = q(\boldsymbol{r}, t)$.

Adiabatic compression or expansion leaves the phase-space density of the CR population unchanged, leading to a momentum shift according to $p \rightarrow p' = (\rho/\rho_0)^{1/3}\, p$ for a change in gas density from ρ_0 to ρ. Since this is fully reversible, it is useful to introduce the invariant cut-off and normalization q_0 and C_0 which describe the CR population via equation (2.1) if the interstellar medium (ISM) or ICM is adiabatically compressed or expanded to the reference density ρ_0. The actual parameters are then given by

$$q(\rho) = \left(\frac{\rho}{\rho_0}\right)^{1/3} q_0 \quad \text{and} \quad C(\rho) = \left(\frac{\rho}{\rho_0}\right)^{(\alpha+2)/3} C_0. \tag{2.2}$$

These adiabatically invariant variables are a suitable choice to be used in a Lagrangian description of the CR population.

[1] Gamma-ray Large Area Space Telescope (GLAST), http://glast.gsfc.nasa.gov/

[2] Low Frequency Array (LOFAR), http://www.lofar.org/

[3] α-particles carry a significant fraction of the total CR energy. Nevertheless, the assumption of considering only CR protons is a reasonable approximation, since the energy density of α-particles can be absorbed into the proton spectrum. A GeV-energy α-particle can be approximated as an ensemble of four individual nucleons travelling together due to the relatively weak MeV nuclear-binding energies compared to the kinetic energy of relativistic protons.

The CR number density is

$$n_{\rm CR} = \int_0^\infty {\rm d}p\, f(p) = \frac{C\, q^{1-\alpha}}{\alpha - 1}, \tag{2.3}$$

provided that $\alpha > 1$. The kinetic energy density of the CR population is

$$\varepsilon_{\rm CR} = \int_0^\infty {\rm d}p\, f(p)\, T_{\rm p}(p) = \frac{C\, m_{\rm p} c^2_{\rm light}}{\alpha - 1} \times \left[\frac{1}{2}\, \mathcal{B}_{1/(1+q^2)}\left(\frac{\alpha-2}{2}, \frac{3-\alpha}{2}\right) + q^{1-\alpha}(\sqrt{1+q^2} - 1)\right], \tag{2.4}$$

where $T_{\rm p}(p) = (\sqrt{1+p^2} - 1)\, m_{\rm p} c^2_{\rm light}$ is the kinetic energy of a proton with momentum p, and $\mathcal{B}_x(a, b)$ denotes the incomplete Beta function which is defined by $\mathcal{B}_x(a, b) \equiv \int_0^x t^{a-1}(1-t)^{b-1}\, {\rm d}t$. The integral of equation (2.4) is well defined if we assume $\alpha > 2$. The CR pressure is

$$P_{\rm CR} = \frac{m_{\rm p} c^2_{\rm light}}{3} \int_0^\infty {\rm d}p\, f(p)\, \beta p = \frac{C\, m_{\rm p} c^2_{\rm light}}{6}\, \mathcal{B}_{1/(1+q^2)}\left(\frac{\alpha-2}{2}, \frac{3-\alpha}{2}\right), \tag{2.5}$$

where $\beta \equiv \upsilon / c_{\rm light} = p/\sqrt{1+p^2}$ is the dimensionless velocity of the CR particle. Note that for $2 < \alpha < 3$ the kinetic energy density and pressure of the CR populations are well defined for the limit $q \to 0$, although the total CR number density diverges.

The adiabatic exponent of the CR population is defined by

$$\gamma_{\rm CR} \equiv \left.\frac{{\rm d}\log P_{\rm CR}}{{\rm d}\log \rho}\right|_S, \tag{2.6}$$

while the derivative has to be taken at constant entropy S. Using equations (2.2) and (2.5), we obtain for the CR adiabatic exponent

$$\gamma_{\rm CR} = \frac{\rho}{P_{\rm CR}}\left(\frac{\partial P_{\rm CR}}{\partial C}\frac{\partial C}{\partial \rho} + \frac{\partial P_{\rm CR}}{\partial q}\frac{\partial q}{\partial \rho}\right) = \frac{\alpha+2}{3} - \frac{2}{3}\, q^{2-\alpha}\, \beta(q)\left[\mathcal{B}_{1/(1+q^2)}\left(\frac{\alpha-2}{2}, \frac{3-\alpha}{2}\right)\right]^{-1}. \tag{2.7}$$

Note that in contrast to the usual adiabatic exponent, the CR adiabatic exponent is time dependent due to its dependence on the lower cut-off of the CR population, q. The ultrarelativistic limit ($q \to \infty$) of the adiabatic exponent, where $\gamma_{\rm CR} \to 4/3$, can easily be obtained by using the integral representation of the incomplete Beta function and applying a Taylor expansion to the integrand. In the non-relativistic limit ($q \ll 1$ and $\alpha > 3$), the adiabatic exponent approaches $\gamma_{\rm CR} \to 5/3$. This can be seen by evaluating the CR pressure in this limit, $P_{\rm CR} = \frac{m_{\rm p} c^2_{\rm light}}{3(\alpha-3)}\, C q^{3-\alpha}$ and applying the definition of $\gamma_{\rm CR}$ in equation (2.6). Considering a composite of thermal and CR gas, it is appropriate to define an effective adiabatic index by

$$\gamma_{\rm eff} \equiv \left.\frac{{\rm d}\log(P_{\rm th} + P_{\rm CR})}{{\rm d}\log \rho}\right|_S = \frac{\gamma_{\rm th}\, P_{\rm th} + \gamma_{\rm CR}\, P_{\rm CR}}{P_{\rm th} + P_{\rm CR}}. \tag{2.8}$$

3 MACH NUMBERS WITHIN THE SPH FORMALISM

The shock surface separates two regions: the *upstream regime* (pre-shock regime) defines the region in front of the shock whereas the *downstream regime* (post-shock regime) defines the wake of the shock wave. The shock front itself is the region in which the mean plasma velocity changes rapidly on small scales given by plasma physical processes. All calculations in this section are done in the rest frame of the shock which we assume to be non-relativistic. This assumption is justified in the case of cosmological structure formation shock waves for which typical shock velocities are of the order of $10^3\,{\rm km\,s^{-1}}$.

Particles are impinging on the shock surface at a rate per unit shock surface, j, while conserving their mass:

$$\rho_1 \upsilon_1 = \rho_2 \upsilon_2 = j. \tag{3.1}$$

Here, υ_1 and υ_2 indicate the plasma velocities (relative to the rest frame of the shock) in the upstream and downstream regime of the shock, respectively. The mass densities in the respective shock regime are denoted by ρ_1 and ρ_2. Momentum conservation implies

$$P_1 + \rho_1 \upsilon_1^2 = P_2 + \rho_2 \upsilon_2^2, \tag{3.2}$$

where P_i denotes the pressure in the respective regime $i \in \{1, 2\}$. The energy-conservation law at the shock surface reads

$$(\varepsilon_1 + P_1)\, \rho_1^{-1} + \frac{\upsilon_1^2}{2} = (\varepsilon_2 + P_2)\, \rho_2^{-1} + \frac{\upsilon_2^2}{2}. \tag{3.3}$$

ε_i denotes the internal energy density in the regime $i \in \{1, 2\}$. Combining solely these three equations without using any additional information about the equation of state, we arrive at the following system of two equations:

$$j^2 = \rho_1^2 \mathcal{M}_1^2 c_1^2 = \frac{(P_2 - P_1)\, \rho_1 \rho_2}{\rho_2 - \rho_1} \tag{3.4}$$

$$\frac{\rho_2}{\rho_1} = \frac{2\varepsilon_2 + P_1 + P_2}{2\varepsilon_1 + P_1 + P_2}. \tag{3.5}$$

Here, we introduced the Mach number in the upstream regime, $\mathcal{M}_1 = \upsilon_1 / c_1$, which is the plasma velocity in units of the local sound speed $c_1 = \sqrt{\gamma P_1 / \rho_1}$.[4]

3.1 Polytropic gas

Non-radiative polytropic gas in the regime $i \in \{1, 2\}$ is characterized by its particular equation of state,

$$\varepsilon_i = \frac{1}{\gamma - 1} P_i \qquad \text{or equivalently} \quad P_i = P_0 \left(\frac{\rho_i}{\rho_0}\right)^\gamma, \tag{3.6}$$

where γ denotes the adiabatic index. This allows us to derive the well-known Rankine–Hugoniot conditions which relate quantities from the upstream to the downstream regime solely as a function of $\mathcal{M}_1$:

$$\frac{\rho_2}{\rho_1} = \frac{(\gamma+1)\mathcal{M}_1^2}{(\gamma-1)\mathcal{M}_1^2 + 2}, \tag{3.7}$$

$$\frac{P_2}{P_1} = \frac{2\gamma\mathcal{M}_1^2 - (\gamma-1)}{\gamma+1}, \tag{3.8}$$

$$\frac{T_2}{T_1} = \frac{\left[2\gamma\mathcal{M}_1^2 - (\gamma-1)\right]\left[(\gamma-1)\mathcal{M}_1^2 + 2\right]}{(\gamma+1)^2 \mathcal{M}_1^2}. \tag{3.9}$$

[4] Note that the symbol c (sometimes with subscript) denotes the sound velocity.

In cosmological simulations using a Lagrangian description of hydrodynamics such as SPH, it is infeasible to identify the rest frame of each shock and thus $\mathcal{M}_1$ unambiguously, especially in the presence of multiple oblique structure formation shocks. As an approximate solution, we rather propose the following procedure, which takes advantage of the entropy-conserving formulation of SPH (Springel & Hernquist 2002). For one particle, the instantaneous injection rate of the entropic function due to shocks is computed, i.e. $\mathrm{d}A/\mathrm{d}t$, where A denotes the entropic function $A(s)$ defined by

$$P = A(s)\rho^{\gamma}, \tag{3.10}$$

and s gives the specific entropy. Suppose further that the shock is broadened to a scale of order the SPH smoothing length $f_h h$, where $f_h \sim 2$ denotes a factor which has to be calibrated against shock tubes. We can roughly estimate the time it takes for the particle to pass through the broadened shock front as $\Delta t = f_h h/\upsilon$, where one may approximate υ with the pre-shock velocity υ_1. Assuming that the present particle temperature is a good approximation for the pre-shock temperature, we can also replace υ_1 with $\mathcal{M}_1 c_1$.[5]

Based on these assumptions and using $\Delta A_1 \simeq \Delta t\, \mathrm{d}A_1/\mathrm{d}t$, one can estimate the jump of the entropic function the particle will receive while passing through the shock:

$$\frac{A_2}{A_1} = \frac{A_1 + \Delta A_1}{A_1} = 1 + \frac{f_h h}{\mathcal{M}_1 c_1 A_1}\frac{\mathrm{d}A_1}{\mathrm{d}t}, \tag{3.11}$$

$$\frac{A_2}{A_1} = \frac{P_2}{P_1}\left(\frac{\rho_1}{\rho_2}\right)^{\gamma} = f_A(\mathcal{M}_1), \tag{3.12}$$

where

$$f_A(\mathcal{M}_1) \equiv \frac{2\gamma\mathcal{M}_1^2 - (\gamma-1)}{\gamma+1}\left[\frac{(\gamma-1)\mathcal{M}_1^2 + 2}{(\gamma+1)\mathcal{M}_1^2}\right]^{\gamma}, \tag{3.13}$$

using equations (3.7) and (3.8). Combining equations (3.11) and (3.12), we arrive at the final equation which is a function of Mach number only:

$$[f_A(\mathcal{M}_1) - 1]\,\mathcal{M}_1 = \frac{f_h h}{c_1 A_1}\frac{\mathrm{d}A_1}{\mathrm{d}t}. \tag{3.14}$$

The right-hand side can be estimated individually for each particle, and the left-hand side depends only on $\mathcal{M}_1$. Determining the root of the equation hence allows one to estimate a Mach number for each particle.

3.2 Composite of cosmic rays and thermal gas

In the presence of a gas composed of CRs and thermal components, equations (3.1)–(3.5) are still applicable if one identifies the energy density ε_i and the pressure P_i with the sum of the individual components in the regime $i \in \{1, 2\}$,

$$\varepsilon_i = \varepsilon_{\mathrm{CR}i} + \varepsilon_{\mathrm{th}i}, \tag{3.15}$$

$$P_i = P_{\mathrm{CR}i} + P_{\mathrm{th}i}. \tag{3.16}$$

The sound speed of such a composite gas is $c_i = \sqrt{\gamma_{\mathrm{eff},i} P_i/\rho_i}$, where $\gamma_{\mathrm{eff},i}$ is given by equation (2.8). Note that in contrast to the single-component fluid, for the general case there is no equivalent to the equation of state (equation 3.6) in terms of the total energy density ε_i, because of the additivity of both pressure and energy density. For later convenience, we introduce the shock compression ratio x_{s} and the thermal pressure ratio y_{s},

$$x_{\mathrm{s}} = \frac{\rho_2}{\rho_1} \quad \text{and} \quad y_{\mathrm{s}} = \frac{P_{\mathrm{th}2}}{P_{\mathrm{th}1}}. \tag{3.17}$$

While taking the equation of state (equation 3.6) for the thermal gas component, we assume adiabatic compression of the CRs at the shock,[6]

$$P_{\mathrm{CR}2} = P_{\mathrm{CR}1} x_{\mathrm{s}}^{\gamma_{\mathrm{CR}}} \quad \text{and} \quad \varepsilon_{\mathrm{CR}2} = \varepsilon_{\mathrm{CR}1} x_{\mathrm{s}}^{\gamma_{\mathrm{CR}}}. \tag{3.18}$$

Here, we assume a constant CR spectral index over the shock which holds only approximately owing to the weak dependence of the CR lower-momentum cut-off q on the density (equation 2.2).

For the composite of thermal and CR gas, it is convenient to define the effective entropic function A_{eff} and its time derivative,

$$A_{\mathrm{eff}} = (P_{\mathrm{th}} + P_{\mathrm{CR}})\rho^{-\gamma_{\mathrm{eff}}}, \tag{3.19}$$

$$\frac{\mathrm{d}A_{\mathrm{eff}}}{\mathrm{d}t} = \frac{\mathrm{d}A_{\mathrm{th}}}{\mathrm{d}t}\rho^{\gamma_{\mathrm{th}}-\gamma_{\mathrm{eff}}}. \tag{3.20}$$

The expression for the time derivative of the effective adiabatic function uses the approximation of adiabatic compression of the CRs at the shock. Using the same assumptions like in the non-radiative case, we estimate the jump of the entropic function for the particle on passing through the shock made of composite gas:

$$\frac{A_{\mathrm{eff},2}}{A_{\mathrm{eff},1}} = \frac{(P_{\mathrm{CR}2} + P_{\mathrm{th}2})\rho_2^{-\gamma_{\mathrm{eff},2}}}{(P_{\mathrm{CR}1} + P_{\mathrm{th}1})\rho_1^{-\gamma_{\mathrm{eff},1}}} = 1 + \frac{f_h h}{\mathcal{M}_1 c_1 A_{\mathrm{eff},1}}\frac{\mathrm{d}A_{\mathrm{eff},1}}{\mathrm{d}t}. \tag{3.21}$$

Combining equations (3.4), (3.5), (3.18) and (3.21), we arrive at the following system of equations:

$$\begin{aligned} f_1(x_{\mathrm{s}}, y_{\mathrm{s}}) = {} & x_{\mathrm{s}}[P_2(x_{\mathrm{s}}, y_{\mathrm{s}}) - P_1] \\ & \times \left[P_2(x_{\mathrm{s}}, y_{\mathrm{s}})(x_{\mathrm{s}}\rho_1)^{-\gamma_{\mathrm{eff},2}(x_{\mathrm{s}}, y_{\mathrm{s}})} - P_1\rho_1^{-\gamma_{\mathrm{eff},1}}\right]^2 \\ & - P_1^2(x_{\mathrm{s}} - 1)\,\rho_1^{1-2\gamma_{\mathrm{eff},1}}\left(\frac{f_h h}{A_{\mathrm{eff},1}}\frac{\mathrm{d}A_{\mathrm{eff},1}}{\mathrm{d}t}\right)^2 = 0, \end{aligned} \tag{3.22}$$

$$\begin{aligned} f_2(x_{\mathrm{s}}, y_{\mathrm{s}}) = {} & 2\varepsilon_2(x_{\mathrm{s}}, y_{\mathrm{s}}) + P_1 + P_2(x_{\mathrm{s}}, y_{\mathrm{s}}) \\ & - x_{\mathrm{s}}\,[2\varepsilon_1 + P_1 + P_2(x_{\mathrm{s}}, y_{\mathrm{s}})] = 0. \end{aligned} \tag{3.23}$$

The effective adiabatic index in the post-shock regime is given by

$$\gamma_{\mathrm{eff},2}(x_{\mathrm{s}}, y_{\mathrm{s}}) = \frac{\gamma_{\mathrm{CR}} P_{\mathrm{CR}2}(x_{\mathrm{s}}) + \gamma_{\mathrm{th}} y_{\mathrm{s}} P_{\mathrm{th}1}}{P_2(x_{\mathrm{s}}, y_{\mathrm{s}})}. \tag{3.24}$$

Given all the quantities in the pre-shock regime, we can solve for the roots x_{s} and y_{s} of this system of two non-linear equations. This system of equations turns out to be nearly degenerate for plausible values of pre-shock quantities such that it might be convenient to apply the following coordinate transformation:

$$(x_{\mathrm{s}}, y_{\mathrm{s}}) \rightarrow (x_{\mathrm{s}}, z_{\mathrm{s}}) \quad \text{with} \quad z_{\mathrm{s}} = \frac{y_{\mathrm{s}} - x_{\mathrm{s}}}{4}. \tag{3.25}$$

The Mach number $\mathcal{M}_1$ and the jump of internal specific energies can then be obtained by

$$\mathcal{M}_1 = \sqrt{\frac{(P_2 - P_1)x_{\mathrm{s}}}{\rho_1 c_1^2(x_{\mathrm{s}} - 1)}} \quad \text{and} \tag{3.26}$$

$$\frac{u_2}{u_1} = \frac{y_{\mathrm{s}}}{x_{\mathrm{s}}} \quad \text{where} \quad u = \frac{P_{\mathrm{th}}}{(\gamma_{\mathrm{th}} - 1)\,\rho}. \tag{3.27}$$

[5] Extensions of this approach that apply to particles within the SPH-broadened shock surface will be described in Section 4.1.

[6] Due to their much larger gyro radii and high velocities, CR protons should not participate in the plasma processes of collisionless shock waves.

4 NUMERICAL IMPLEMENTATION

4.1 Polytropic gas

Applying the algorithm of inferring the shock strength within the SPH formalism in a straightforward manner will lead to systematically underestimated values of the Mach number for SPH particles which are located *within the SPH-broadened shock surface*: the proposed algorithm of Section 3 assumes that the present particle quantities such as entropy, sound velocity and smoothing length are good representations of the hydrodynamical state in the pre-shock regime, which is no longer the case for particles within the SPH-broadened shock surface. To overcome this problem, we define a decay time interval $\Delta t_{\rm dec} = \min[f_h h/(\mathcal{M}_1 c), \Delta t_{\rm max}]$, during which the Mach number is set to the maximum value that is estimated during the transition from the pre-shock regime to the shock surface. At this maximum, the corresponding particle quantities are good approximations of the hydrodynamical values in the pre-shock regime. We thus have a finite temporal resolution for detecting shocks, which is of order of the transit time through the broadened shock front. Note that $\Delta t_{\rm max}$ is just introduced as a safeguard against too long decay times for very weak shocks. In the case of cosmological simulations, which are conveniently carried out in a computational domain that is comoving with the cosmological expansion, we redefine the decay time $\Delta(\ln a)_{\rm dec} = \min[H(a) f_h h/(\mathcal{M}_1 c), \Delta(\ln a)_{\rm max}]$ where a denotes the cosmic scalefactor $H(a) = \dot{a}/a$ is the Hubble function. An appropriate choice for the safeguard parameter is $\Delta\,(\ln a)_{\rm max} = 0.0025$.

Secondly, there is no universal value f_h which measures the SPH shock broadening accurately irrespective of the Mach number of the shock, especially in the regime of strong shocks. We therefore use the original algorithm (with $f_h = 2$) only for estimated Mach numbers with $\mathcal{M}_{\rm est} < 3$, while for stronger shocks, we apply an empirically determined formula (calibrated against shock tubes) which corrects for the additional broadening of strong shocks and smoothly joins into the weak shock regime:

$$\mathcal{M}_{\rm cal} = \left(a_{\mathcal{M}} \mathcal{M}_{\rm est}^{b_{\mathcal{M}}} + c_{\mathcal{M}}\, {\rm e}^{-\mathcal{M}_{\rm est}/3}\right) \mathcal{M}_{\rm est}, \tag{4.1}$$

where $a_{\mathcal{M}} = 0.09$, $b_{\mathcal{M}} = 1.34$ and $c_{\mathcal{M}} = 1.66$. These numbers may depend on the viscosity scheme of the SPH implementation.

4.2 Composite of cosmic rays and thermal gas

Our formalism of inferring the jump conditions for a composite of CRs and thermal gas yields the density jump, $x_{\rm s} = \rho_2/\rho_1$, and the thermal pressure jump at the shock, $y_{\rm s} = P_{\rm th2}/P_{\rm th1}$ (Section 3.2). As described in Section 4.1, the values for the estimated jump conditions are systematically underestimated in the regime of strong shocks ($\mathcal{M}_1 \gtrsim 5$), implying an additional broadening of the shock surface. Thus, we proceed the same way as above: using the value of the density jump $x_{\rm s}$, we derive the Mach number of the shock through equation (3.26) and recalibrate it for strong shocks. In addition, we use the decay time $\Delta t_{\rm dec}$ as before in the thermal case to obtain reliable Mach number estimates. The post-shock density is then obtained by multiplying the stored pre-shock density with the density jump $x_{\rm s}$.

In the case of a thermal pressure jump at the shock $y_{\rm s}$, we decided not to derive another empirical formula but rather exploit CR physics at non-relativistic shocks. Since the CR population is adiabatically compressed at the shock in the limit of strong shocks, the total pressure jump is nearly solely determined by the jump of the thermal pressure in the post-shock regime, i.e. we can safely neglect the contribution of CRs to the pressure jump. This assumption is justified as long as the CR pressure is not dominated by subrelativistic CRs of low energy which is on the other hand a very short-lived population owing to Coulomb interactions in the ICM. Thus, the thermal post-shock pressure for $\mathcal{M}_1 \gtrsim 5$ is estimated as

$$P_{\rm th2} \simeq \frac{2\gamma_{\rm th}\mathcal{M}_1^2 - (\gamma_{\rm th} - 1)}{\gamma_{\rm th} + 1}\, P_1, \tag{4.2}$$

where $\mathcal{M}_1$ is obtained by equation (4.1), and P_1 denotes the stored total pre-shock pressure.

5 SHOCK TUBES

To assess the reliability of our formalism and the validity of our numerical implementation, we perform a sequence of shock-tube simulations with Mach numbers ranging from $\mathcal{M} = 1.4$ to 100. We use a three-dimensional problem set-up which is more demanding and more realistic than carrying out the computation in one dimension. Here and in the following, we drop the subscript '1' of the pre-shock Mach number for convenience. By comparing with known analytic solutions, we are able to demonstrate the validity of our implemented formalism.

There exists an analytic solution of the Riemann shock-tube problem in the case of a fluid described by a polytropic equation of state, $\varepsilon = P/(\gamma - 1)$ (cf. Appendix A). Unfortunately, a composite of thermal gas and CRs does not obey this relation. Thus, we derive an analytic solution to the Riemann shock-tube problem for the composite of CRs and thermal gas in Appendix B. This analytic solution assumes the CR adiabatic index (equation 2.6) to be constant over the shock tube and neglects CR diffusion such that the problem remains analytically treatable.

5.1 Polytropic thermal gas

We consider eight standard shock-tube tests (Sod 1978) which provide a validation of both the code's solution to hydrodynamic problems and our Mach number formalism. We consider first an ideal gas with $\gamma = 5/3$, initially at rest. The left-half space ($x < 250$) is filled with gas at unit density, $\rho_2 = 1$, and $P_2 = (\gamma - 1)\,10^5$, while $x > 250$ is filled with low-density gas ($\rho_1 = 0.2$) at low pressure. The exact value of the low-pressure gas has been chosen such that the resulting solutions yield the Mach numbers $\mathcal{M} = \{1.4, 2, 3, 6, 10, 30, 60, 100\}$ (cf. Appendix A). We set up the initial conditions in three dimensions using an irregular glass-like distribution of a total of 3×10^4 particles of equal mass in hydrostatic equilibrium. They are contained in a periodic box which is longer in x-direction than in the other two dimensions, y and z.

In the left-hand panel of Fig. 1, we show the result for the case of the Mach number $\mathcal{M} = 10$ obtained with the GADGET-2 code (Springel, Yoshida & White 2001; Springel 2005) at time $t = 0.5$. Shown are the volume-averaged hydrodynamical quantities $\langle\rho(x)\rangle$, $\langle P(x)\rangle$, $\langle v_x(x)\rangle$ and $\langle\mathcal{M}(x)\rangle$ within bins with a spacing equal to the interparticle separation of the denser medium and represented by solid black lines. One can clearly distinguish five regions of gas with different hydrodynamical states. These regions are separated by the head and the tail of the leftwards propagating rarefaction wave, and the rightwards propagating contact discontinuity and the shock wave. The overall agreement with the analytic solution is good, while the discontinuities are resolved within 2–3 SPH smoothing lengths. Despite the shock broadening, the post-shock quantities are calculated very accurately. Our formalism is clearly able to detect the shock and precisely measure its strength, i.e. the Mach number $\mathcal{M}$. The pressure quantity drawn is not the hydrodynamically acting

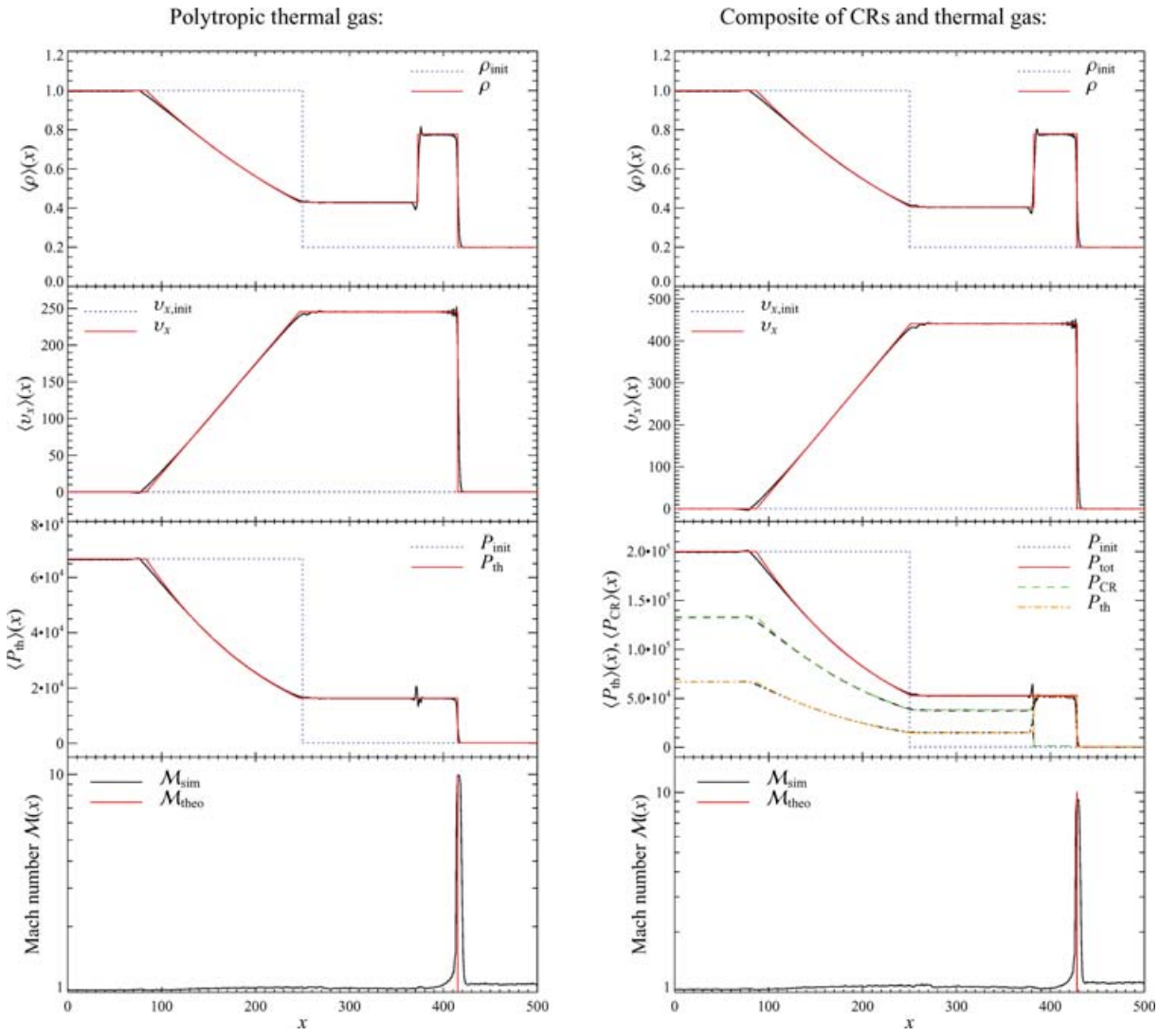

Figure 1. Shock-tube test carried out in a periodic three-dimensional box which is longer in x-direction than in the other two dimensions where a shock with the Mach number $\mathcal{M} = 10$ develops. The numerical result of the volume-averaged hydrodynamical quantities $\langle\rho(x)\rangle$, $\langle P(x)\rangle$, $\langle v_x(x)\rangle$ and $\langle\mathcal{M}(x)\rangle$ within bins with a spacing equal to the interparticle separation of the denser medium is shown in black and compared with the analytic result in colour. Left-hand panels: shock tubes are filled with pure thermal gas ($\gamma = 5/3$). Right-hand panels: shock tubes are filled with a composite of CRs and thermal gas. Initially, the relative CR pressure is $X_{\rm CR} = P_{\rm CR}/P_{\rm th} = 2$ in the left-half space ($x < 250$), while we assume pressure equilibrium between CRs and thermal gas for $x > 250$.

pressure of the SPH dynamics but $P = (\gamma - 1)\rho u$, a product of two fields that are calculated each using SPH interpolation. Thus, the observed characteristic pressure blip at the contact discontinuity has no real analogue either in the averaged x-component of the velocity $\langle v_x(x)\rangle$ or in the averaged Mach number $\langle\mathcal{M}(x)\rangle$. The x-component of the velocity $\langle v_x(x)\rangle$ shows tiny post-shock oscillations which might be damped with higher values of the artificial viscosity in the expense of a broader shock surface. The leftwards propagating rarefaction wave seems to exhibit a slightly faster signal velocity compared to the sound velocity. This might be attributed to the SPH averaging process which obtains additional information on the SPH smoothing scale.

In the left-hand panel of Fig. 2, we show the Mach number distributions weighted by the change of dissipated energy per time interval, $\langle {\rm d}\dot{u}_{\rm th}/({\rm d}\log\mathcal{M})\rangle$ for our eight shock tubes. The sharp peaks of these distributions around their expected values $\log\mathcal{M}$ are apparent. This demonstrates the reliability of our formalism to precisely measure shock strengths instantaneously during SPH simulations. The bottom panel shows their integral, i.e. the change of dissipated energy per time interval, $\langle\dot{u}_{\rm th}\rangle$. The rising dissipated energy with growing Mach number reflects the larger amount of available kinetic energy for dissipation.

We additionally calculate the shock-injected CR energy using the formalism of DSA described in Enßlin et al. (in preparation). However, the injected CR energy $\langle\dot{u}_{\rm CR,inj}\rangle$ was only monitored and not dynamically tracked. For comparison, we also show the theoretically expected injected CR energy $\langle\dot{u}^{\rm theory}_{\rm CR,inj}\rangle = \zeta_{\rm inj}\langle\dot{u}_{\rm th}\rangle$, where $\zeta_{\rm inj}$ is the energy efficiency due to DSA (cf. Enßlin et al. in preparation, for details). The good comparison of the simulated and theoretically expected shock-injected CR energy demonstrates that our formalism is reliably able to describe the on-the-fly acceleration of CRs during the simulation.

5.2 Composite of cosmic rays and thermal gas

Again, we consider eight shock-tube simulations containing a composite of CRs and thermal gas, providing a useful validation of

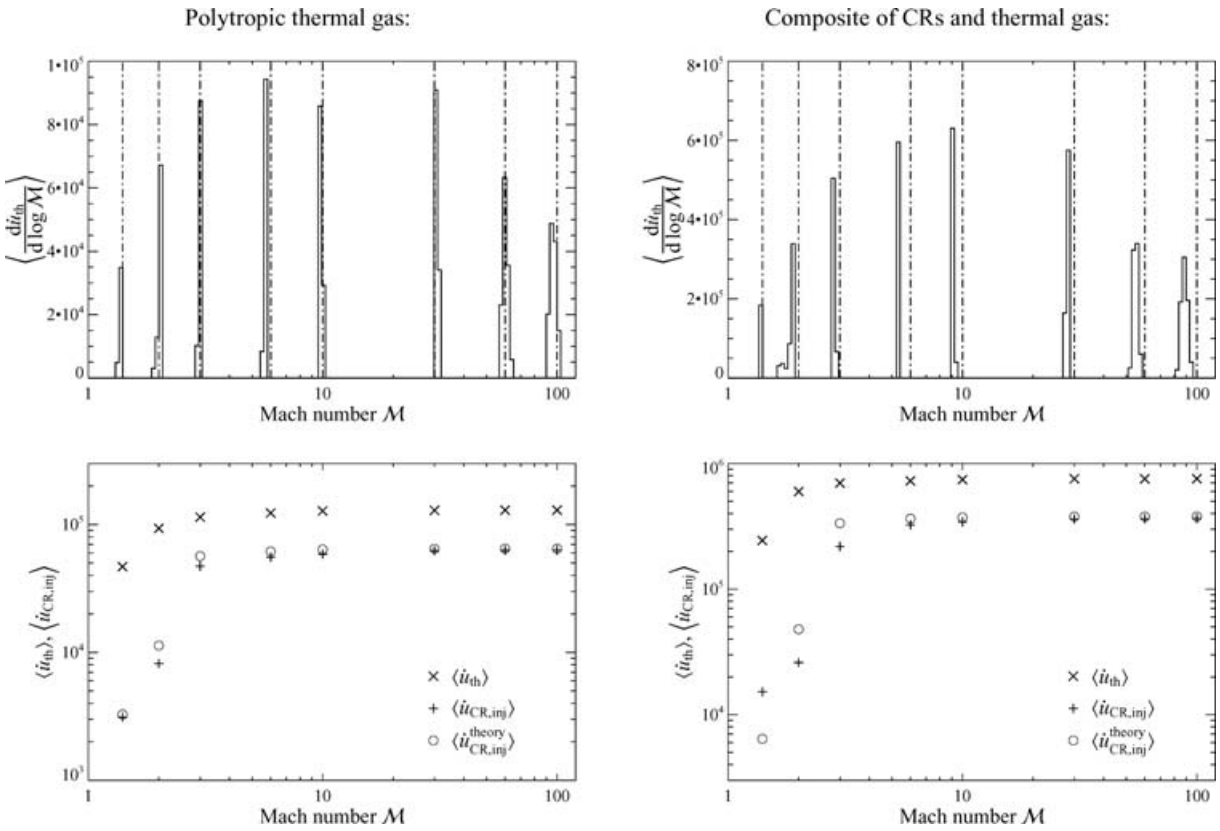

Figure 2. Mach number distributions weighted by the change of dissipated energy per time interval, $\langle {\rm d}\dot{u}_{\rm th}/({\rm d}\log\mathcal{M})\rangle$ for our eight three-dimensional shock tubes. Left-hand panels: shock tubes are filled with pure thermal gas ($\gamma = 5/3$). Right-hand panels: shock tubes are filled with a composite of CRs and thermal gas. Initially, the relative CR pressure is $X_{\rm CR} = P_{\rm CR}/P_{\rm th} = 2$ in the left-half space, while we assume pressure equilibrium between CRs and thermal gas. Bottom panels: Shown are the change of dissipated energy per time interval, $\langle \dot{u}_{\rm th}\rangle$ (shown with $\times$), the shock-injected CR energy $\langle \dot{u}_{\rm CR,inj}\rangle$ (+) and the theoretically expected injected CR energy $\langle \dot{u}^{\rm theory}_{\rm CR,inj}\rangle$(○) which is calculated following Enßlin et al. (in preparation).

our CR implementation in solving basic hydrodynamic problems as well as our Mach number formalism in the presence of CRs. In these simulations, we neither inject shock-accelerated CRs nor consider CR diffusion: these processes would lead to CR-modified shock structures and shall be the subject of a companion paper.

To characterize this composite fluid, we define the relative CR pressure $X_{\rm CR} = P_{\rm CR}/P_{\rm th}$. Our composite gas is initially at rest, while the left-half space ($x < 250$) is filled with gas at unit density, $\rho_2 = 1$, $X_{\rm CR2} = 2$ and $P_{\rm th2} = (\gamma - 1)\,10^5$, while $x > 250$ is filled with low-density gas, $\rho_1 = 0.2$, $X_{\rm CR1} = 1$, at low pressure. The exact value of the low-pressure gas has again been chosen such that the resulting solutions yield the Mach numbers $\mathcal{M} = \{1.4, 2, 3, 6, 10, 30, 60, 100\}$ (cf. Appendix B). Otherwise, we use the same initial set-up as in Section 5.1. This CR load represents a rather extreme case and can be taken as the limiting case for our Mach number formalism in the presence of CRs. Cosmologically, it may find application in galaxy mergers where the outer regions might be composed of an adiabatically expanded composite gas containing a high CR component.

In the right-hand panel of Fig. 1, we show the result for the case of the Mach number $\mathcal{M} = 10$ obtained with GADGET-2 at time $t = 0.3$. The agreement with the analytic solution is good, while the discontinuities are resolved within 2–3 SPH smoothing lengths. Despite the shock broadening, the post-shock quantities are calculated very accurately. In the case of composite gas, our formalism is clearly able to detect the shock and measure its strength with a Mach number accuracy better than 10 per cent. Although the total pressure remains constant across the contact discontinuity, the partial pressure of CRs and thermal gas interestingly are changing. This behaviour reflects the adiabatic compression of the CR pressure component across the shock wave. A posteriori, this justifies our procedure of inferring the thermal pressure jump at the shock for a composite of CRs and thermal gas in equation (4.2).

In the right-hand panel of Fig. 2, we show the Mach number distributions weighted by the change of dissipated energy per time interval, $\langle {\rm d}\dot{u}_{\rm th}/({\rm d}\log\mathcal{M})\rangle$ for our eight shock tubes. While our formalism is able to measure the shock strength with a Mach number accuracy better than 10 per cent, the distributions are sharply peaked. This demonstrates the reliability of our formalism to measure shock strengths for the composite gas instantaneously during SPH simulations.

The bottom panel shows the change of dissipated energy per time interval, $\langle \dot{u}_{\rm th}\rangle$ together with the shock-injected CR energy $\langle \dot{u}_{\rm CR,inj}\rangle$. Concerning the amount of injected CR energy, we neglected cooling processes such as Coulomb interactions with thermal particles: this would effectively result in a density-dependent recalibration of the maximum CR energy efficiency $\zeta_{\rm max}$ of the otherwise arbitrary absolute value of our fiducial density. In the case of high Mach numbers, there is a good agreement between the simulated and theoretically expected shock-injected CR energy while there are discrepancies at low Mach numbers: our formalism estimates volume-averaged Mach numbers with an accuracy better than 10 per cent; this uncertainty translates to estimates of the density jump $x_{\rm s}$ and the thermal

pressure jump y_s with a scatter among different SPH particles. In the regime of weak shocks, the CR energy efficiency due to DSA $\zeta_{\rm inj}$ is extremely sensitive to these two quantities, leading to larger uncertainties for the shock-injected CR energy in the case of a high CR load. However, the overall trend for the shock-injected CR energy can still be matched in such an extreme physical environment.

6 NON-RADIATIVE COSMOLOGICAL SIMULATIONS

6.1 Simulation set-up

As a first application of our formalism, we are here interested in studying the spatial distribution of cosmological structure formation shocks in combination with Mach number statistics. We focus on the 'concordance' cosmological cold dark matter model with a cosmological constant (ΛCDM). The cosmological parameters of our model are: $\Omega_{\rm m} = \Omega_{\rm dm} + \Omega_{\rm b} = 0.3$, $\Omega_{\rm b} = 0.04$, $\Omega_\Lambda = 0.7$, $h = 0.7$, $n = 1$ and $\sigma_8 = 0.9$. Here, $\Omega_{\rm m}$ denotes the total matter density in units of the critical density for geometrical closure, $\rho_{\rm crit} = 3H_0^2/(8\pi G)$. $\Omega_{\rm b}$ and Ω_Λ denote the densities of baryons and the cosmological constant at the present day. The Hubble constant at the present day is parametrized as $H_0 = 100\,h\,{\rm km\,s^{-1}\,Mpc^{-1}}$, while n denotes the spectral index of the primordial power spectrum and σ_8 is the *rms* linear mass fluctuation within a sphere of radius $8\,h^{-1}$ Mpc extrapolated to $z = 0$. This model yields a reasonable fit to current cosmological constraints and provides a good framework for investigating cosmological shocks.

Our simulations were carried out with an updated and extended version of the distributed-memory parallel TreeSPH code GADGET-2 (Springel et al. 2001; Springel 2005) including now self-consistent CR physics (Enßlin et al. in preparation; Jubelgas et al. in preparation). Our reference simulation employed 2×256^3 particles which were simulated within a periodic box of comoving size $100\,h^{-1}$ Mpc, so the dark matter particles had masses of $4.3 \times 10^9\,h^{-1}\,{\rm M}_\odot$ and the SPH particles $6.6 \times 10^8\,h^{-1}\,{\rm M}_\odot$. The SPH densities were computed from 32 neighbours which leads to our minimum gas resolution of approximately $2 \times 10^{10}\,h^{-1}\,{\rm M}_\odot$. The gravitational force softening was of a spline form (e.g. Hernquist & Katz 1989) with a Plummer-equivalent softening length of $13\,h^{-1}$ kpc comoving. In order to test our numerical resolution, we additionally simulated the same cosmological model with 2×128^3 particles, with a softening length twice that of the reference simulation.

Initial conditions were laid down by perturbing a homogeneous particle distribution with a realization of a Gaussian random field with the ΛCDM linear power spectrum. The displacement field in Fourier space was constructed using the Zel'dovich approximation, with the amplitude of each random-phase mode drawn from a Rayleigh distribution. For the initial redshift, we chose $1 + z_{\rm init} = 50$ which translates to an initial temperature of the gas of $T_{\rm init} = 57$ K. This reflects the fact that the baryons are thermally coupled to the CMB photons via Compton interactions with the residual free electrons after the universe became transparent until it eventually decoupled at $1 + z_{\rm dec} \simeq 100(\Omega_{\rm b}h^2/0.0125)^{2/5}$. In all our simulations, we stored the full particle data at 100 output times, equally spaced in $\log(1+z)$ between $z = 40$ and 0.

In order to investigate the effects of reionization on the Mach number statistics, we additionally perform two similar simulations which contain a simple reionization model where we impose a minimum gas temperature of $T = 10^4$ K at a redshift of $z = 10$ to all SPH particles. We decided to adopt this simplified model to study its effect on the Mach number statistics rather than a more complicated reionization history. A more realistic scenario might be to add energy only to gas within haloes above a certain density in combination with energy input from quasi-stellar object (QSO) activity, and to describe the merging of the reionization fronts and their evolution into the lower-density regions (e.g. Ciardi, Stoehr & White 2003).

The simulation reported here follow only non-radiative gas physics. We neglected several physical processes, such as radiative cooling, galaxy/star formation and feedback from galaxies and stars including CR pressure. Our primary focus lies in the shocks that are mostly outside the cluster core regions. Thus, the conclusions drawn in this work should not be significantly weakened by the exclusion of these additional radiative processes.

In contrast to the idealized shock-tube experiment where all particles that are shocked experience the same shock strength, in cosmological simulations there might be a distribution of Mach numbers for a given region of space because of curvature effects, multiple shocks, etc. Thus, the Mach number estimation in shock tubes involves averaging over many particles all of which are experiencing a shock of a given Mach number, whereas in the cosmological simulations the averaging has to be done over Mach number also. This might introduce a scatter to the Mach number estimation of a single particle in cosmological simulations which is difficult to quantify. We are confident that this effect has only a minor impact on our results because they agree well with results of similar studies that used Eulerian structure formation simulations (Ryu et al. 2003).

6.2 Visualization of the Mach number

In the SPH formalism, continuous fields $A(\boldsymbol{x})$ such as the hydrodynamical quantities are represented by the values A_i at discrete particle positions $\boldsymbol{r}_i = (x_i, y_i, z_i)$ with a local spatial resolution given by the SPH smoothing length h_i. To visualize a scalar quantity in two dimensions we employ the mass-conserving *scatter* approach for the projection, where the smoothing kernel of the particle is distributed on to cells of a Cartesian grid which is characterized by its physical mesh size g. The line-of-sight integration of any quantity $A(\boldsymbol{x})$ at the pixel at position $\boldsymbol{r} = (x, y, z)$ is determined as the average of integration of all lines of sight passing through the pixel,

$$\langle a(\boldsymbol{x}_\perp)\rangle_{\rm los} = g^{-2}\sum_i h_i^{-3}\left[\int_{x-g/2}^{x+g/2}{\rm d}x_i\int_{y-g/2}^{y+g/2}{\rm d}y_i \times\int_{-h_i}^{h_i}{\rm d}z_i\,\mathcal{K}\left(\frac{r}{h_i}\right)A_i\right], \tag{6.1}$$

with $r = \sqrt{(x_i - x)^2 + (y_i - y)^2 + z_i^2}$, and where the summation is extended over all particles in the desired slice of projection. The function $\mathcal{K}$ is the dimensionless spherically symmetric cubic spline kernel suggested by Monaghan & Lattanzio (1985).

The left-hand side of Fig. 3 shows the time evolution of the density contrast δ averaged over the line of sight with a comoving projection length $L_{\rm proj} = 10\,h^{-1}$ Mpc:

$$\langle 1 + \delta_{\rm gas}(\boldsymbol{x}_\perp)\rangle_{\rm los} = \frac{\langle\Sigma(\boldsymbol{x}_\perp)\rangle_{\rm los}}{L_{\rm proj}\,\rho_{\rm crit}\,\Omega_{\rm b}}, \tag{6.2}$$

where Σ denotes the surface mass density. The fine-spun cosmic web at high redshift evolves into a much more pronounced, knotty and filamentary structure at late times, as a result of the hierarchical structure formation process driven by gravity.

The right-hand side of Fig. 3 shows the time evolution of the density-weighted temperature averaged over the line of sight. Again, the growth of galaxy clusters visible as large bright regions with

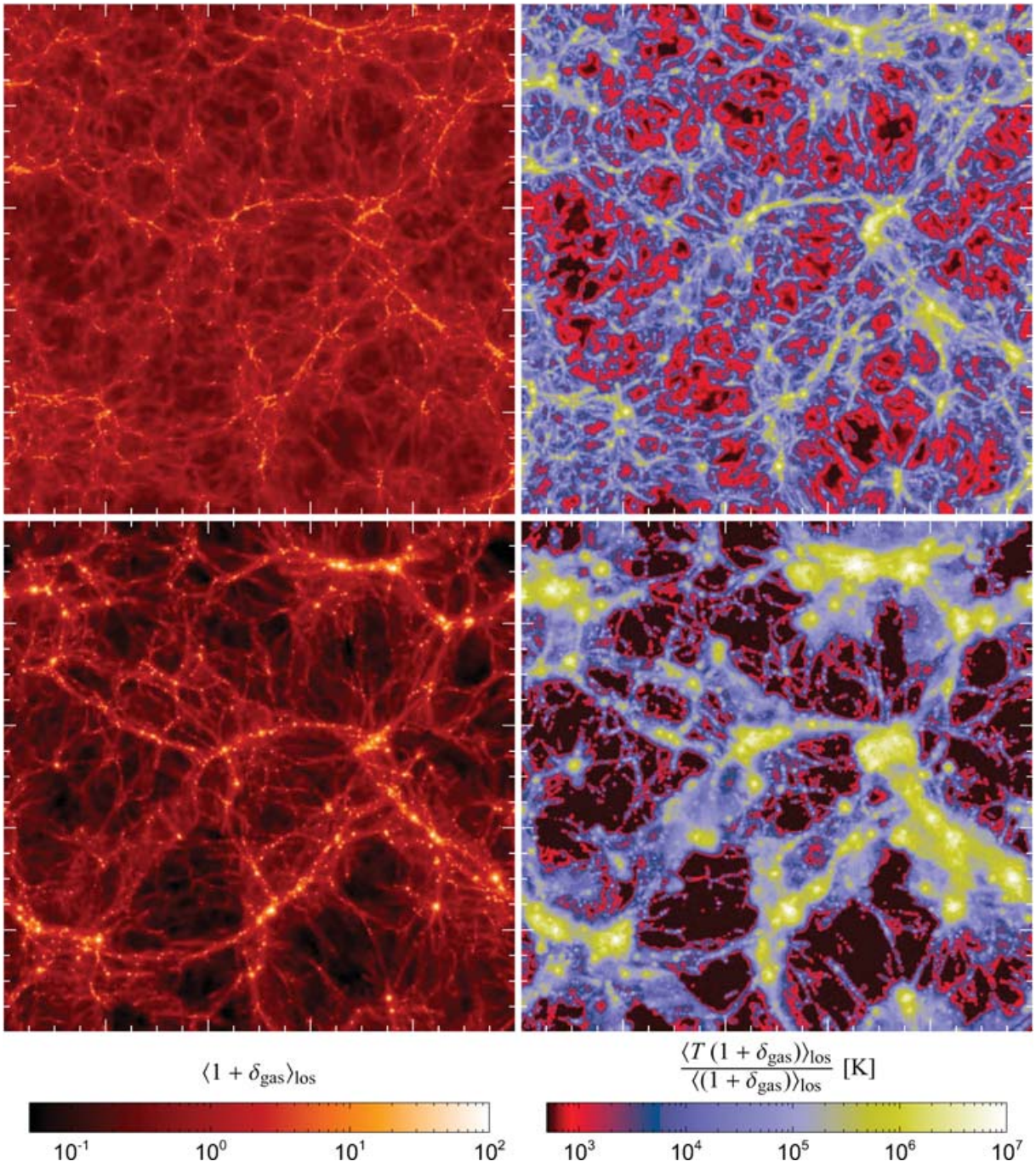

Figure 3. Visualization of a non-radiative cosmological simulation at redshift $z = 2$ (top panels) and $z = 0$ (bottom panels). Shown are the overdensity of the gas (left-hand side) and the density-weighed gas temperature (right-hand side). These pictures have a comoving side length of $100\,h^{-1}$ Mpc while the projection length along the line of sight amounts to $10\,h^{-1}$ Mpc.

temperatures around 10^7 K is clearly visible. Through dissipation, the shock waves convert part of the gravitational energy associated with cosmological structure formation into internal energy of the gas, apart from the additional contribution due to adiabatic compression caused by the material that falls in at later times and itself is compressed at these shock waves. The large black regions show voids which cool down during cosmic evolution due to two effects: while the universe expands, non-relativistic gas is adiabatically expanded and cools according to $T \propto V^{1-\gamma} \propto a^{-2}$ for $\gamma = 5/3$ when shock heating is still absent. Secondly, matter is flowing towards filaments during structure formation, hence the voids get depleted, providing an additional adiabatic expansion of the remaining material.

Fig. 4 shows a visualization of the responsible structure formation shocks and their corresponding strengths. The colour scaling represents the spatial Mach number distribution weighted by the rate of energy dissipation at the shocks, and normalized to the simulation volume (left-hand side). The Mach number distribution weighted

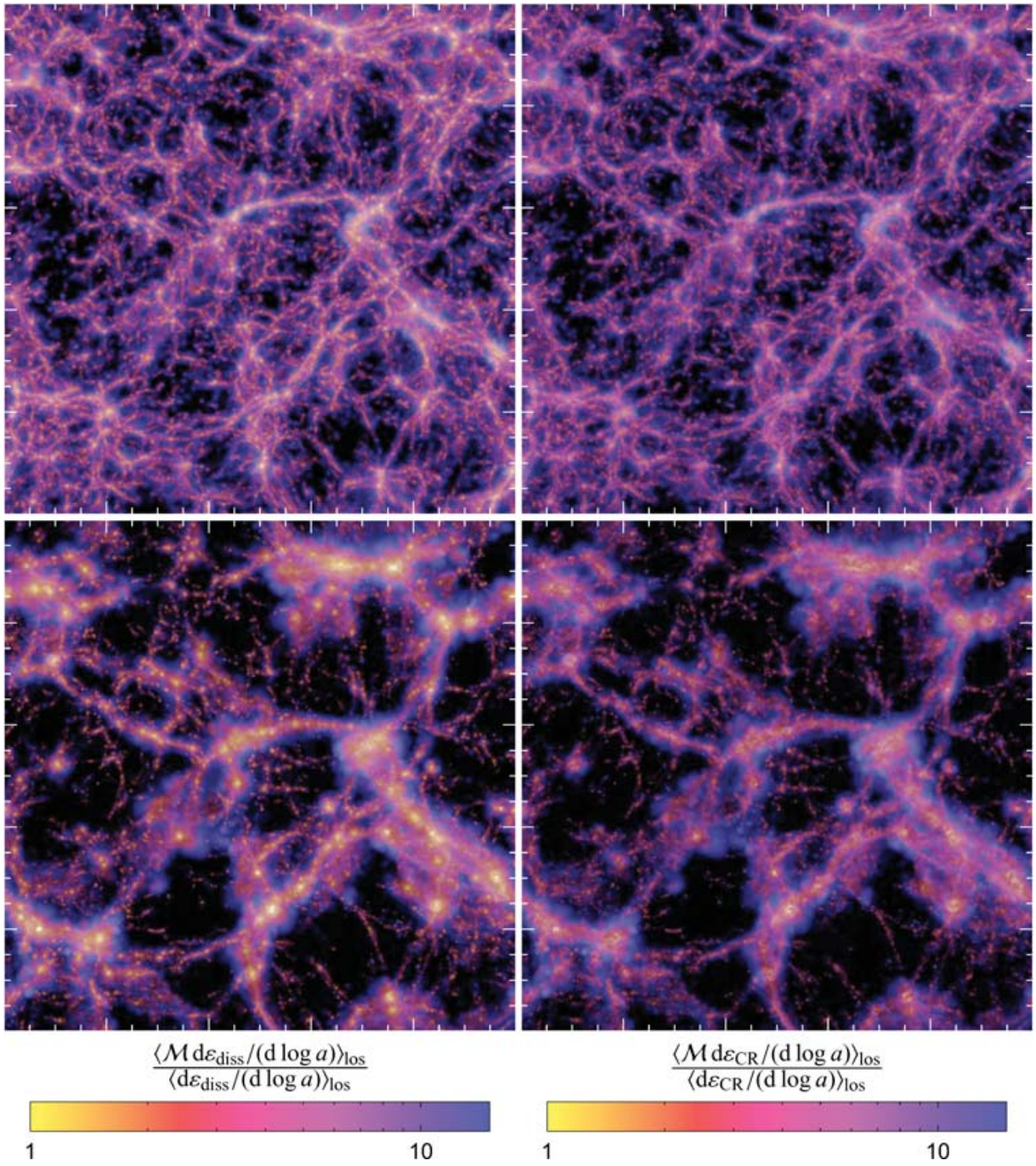

Figure 4. Mach number visualization of a non-radiative cosmological simulation at redshift $z = 2$ (top panels) and $z = 0$ (bottom panels). The colour hue of the maps on the left-hand side encodes the spatial Mach number distribution weighted by the rate of energy dissipation at the shocks, normalized to the simulation volume. The maps on the right-hand side show instead the Mach number distribution weighted by the rate of CR energy injection above $q = 0.8$, the threshold of hadronic interactions. The brightness of each pixel is determined by the respective weights, i.e. by the energy-production density. These pictures have a comoving length of $100\,h^{-1}$ Mpc on a side. Most of the energy is dissipated in weak shocks which are situated in the internal regions of groups or clusters, while collapsed cosmological structures are surrounded by strong external shocks (shown in blue).

by the rate of CR energy injection is shown on the right-hand side, again normalized to the simulation volume. The brightness of these pixels scales with the respective weights, i.e. by the rates of energy dissipation or injection, respectively. The spatial Mach number distribution impressively reflects the non-linear structures and voids of the density and temperature maps of Fig. 3. It is apparent that most of the energy is dissipated in weak shocks which are situated in the internal regions of groups or clusters while collapsed cosmological structures are surrounded by external strong shocks (shown in blue). These external shocks are often referred to as 'first shocks', because here the compressed gas has been processed for the first time in its cosmic history through shock waves.

Following Ryu et al. (2003), we classify structure formation shocks into two broad populations which are labelled as *internal*

and *external* shocks, depending on whether or not the associated pre-shock gas was previously shocked. Rather than using a thermodynamical criterion such as the temperature, we prefer a criterion such as the overdensity δ in order not to confuse the shock definition once we will follow radiatively cooling gas in galaxies (in practice, we use the criterion of a critical pre-shock overdensity $\delta > 10$ for the classification of an internal shock). *External* shocks surround filaments, sheets and haloes while *internal* shocks are located within the regions bound by external shocks and are created by flow motions accompanying hierarchical structure formation. For more detailed studies, internal shocks can be further divided into three types of shock waves: (1) accretion shocks caused by infalling gas from sheets to filaments or haloes and from filaments to haloes, (2) merger shocks resulting from merging haloes and (3) supersonic chaotic flow shocks inside non-linear structures which are produced in the course of hierarchical clustering.

In contrast to the present time, the comoving surface area of external shock waves surpasses that of internal shocks at high redshift, due to the small fraction of mass bound in large haloes and the simultaneous existence of an all-pervading fine-spun cosmic web with large surface area. Also, there the thermal gas has a low sound velocity $c = \sqrt{\gamma P/\rho} = \sqrt{\gamma(\gamma-1)u}$ owing to the low temperature, so once the diffuse gas breaks on mildly non-linear structures, strong shock waves develop that are characterized by high Mach numbers $\mathcal{M} = \upsilon_s/c$. Nevertheless, the energy dissipation rate in internal shocks is always higher compared to external shocks because the mean shock speed and pre-shock gas densities are significantly larger for internal shocks.

We use the same colour and brightness scale for the Mach number distribution weighted by the injected CR energy rate normalized to the simulation volume (right-hand side of Fig. 4). We emphasize two important points which have fundamental implications for the CR population in galaxy clusters. (1) There is an absence of weak shocks (shown in yellow) when the Mach number distribution is weighted by the injected CR energy. This reflects the Mach number-dependent energy-injection efficiency: the CR injection is saturated for strong shocks which leads to similar spatial distribution of both weightings,

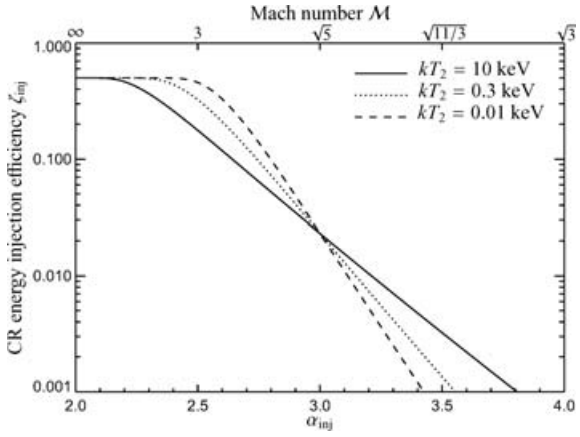

Figure 5. CR energy-injection efficiency for the diffusive shock acceleration process. Shown is the CR energy-injection efficiency $\zeta_{\rm inj} = \varepsilon_{\rm CR}/\varepsilon_{\rm diss}$ for the three post-shock temperatures $kT_2/{\rm keV} = 0.01, 0.3$ and 10. We inject only CRs above the kinematic threshold $q_{\rm threshold} = 0.83$ of the hadronic CR p–p interaction which are able to produce pions that successively decay into secondary electrons, neutrinos and γ-rays. We choose equipartition between injected CR energy and dissipated thermal non-relativistic energy as saturation value of the CR energy-injection efficiency, i.e. $\zeta_{\rm max} = 0.5$ (Ryu et al. 2003).

by dissipated energy as well as by injected CR energy. In contrast, most of the dissipated energy is thermalized in weak shocks and only small parts are used for the acceleration of relativistic particles (compare Fig. 5). (2) The mechanism of energy dissipation at shocks is very density dependent, implying a tight correlation of weak internal shocks and the amount of dissipated energy. This can be seen by the strongly peaked brightness distribution of the dissipated energy rate towards the cluster centres. For the CR-weighted case, this correlation is counteracted by the CR energy-injection efficiency leading to a smoother brightness distribution of the CR energy injection. This has the important implication that the ratio of CR-injected energy to dissipated thermal energy is increasing as the density declines. Relative to the thermal non-relativistic energy density, the CR energy density is dynamically more important at the outer cluster regions and dynamically less important at the cluster centres.

6.3 Mach number statistics

6.3.1 Influence of reionization

To quantify previous considerations, we compute the differential Mach number distribution weighted by the dissipated energy normalized to the simulation volume $\mathrm{d}^2\varepsilon_{\rm diss}(a,\mathcal{M})/(\mathrm{d}\log a\,\mathrm{d}\log\mathcal{M})$ at different redshifts. The top left-hand panel of Fig. 6 shows this Mach number distribution for our reference simulation with reionization (showing a resolution of 2×256^3), while the top right-hand panel shows this distribution for the simulation without reionization. The lower left-hand panel shows both distributions integrated over the scalefactor, $\mathrm{d}\varepsilon_{\rm diss}(\mathcal{M})/(\mathrm{d}\log\mathcal{M})$, in addition to the Mach number distribution weighted by the injected CR energy normalized to the simulation volume, $\mathrm{d}\varepsilon_{\rm CR}(\mathcal{M})/(\mathrm{d}\log\mathcal{M})$ (see Section 6.3.2). Internal shocks are shown with dotted lines and external shocks with dashed lines. The lower right-hand panel shows the evolution of the dissipated energy due to shock waves with scalefactor, $\mathrm{d}\,\varepsilon_{\rm diss}\,(a)/(\mathrm{d}\log a)$, for the models with and without reionization.

Several important points are apparent. (1) The median of the Mach number distribution weighted by the dissipated energy decreases as cosmic time evolves, i.e. the average shock becomes weaker at later times. (2) There is an increasing amount of energy dissipated at shock waves as the universe evolves because the mean shock speed is significantly growing when the characteristic mass becomes larger with time. This trend starts to level off at redshift $z \simeq 1$ although the median Mach number in shocks continuous to decrease. (3) Reionization influences the Mach number distribution predominantly at early times (however after reionization took place) and suppresses strong external shock waves efficiently. The reason is that reionization of the thermal gas increases its sound speed $c = \sqrt{\gamma nkT/\rho}$ dramatically, so that weaker shocks are produced for the same shock velocities. (4) The time-integrated Mach number distribution weighted by the dissipated energy peaks at Mach numbers $1 \lesssim \mathcal{M} \lesssim 3$. The main contribution in terms of energy dissipation originates from internal shocks because of enhanced pre-shock densities and mean shock speeds. (5) External shocks dominate the Mach number distribution at early times while internal shocks take over at $z \simeq 9$ (depending somewhat on the resolution of the simulation). Their amount of dissipated energy surpasses that in external shocks by over an order of magnitude at the present time. Internal shocks play a more important role than external shocks in dissipating energy associated with structure formation.

The total shock-dissipated energy in our simulation box amounts to $E_{\rm diss} = 2.27\times10^{64}$ erg. This translates to a mean energy

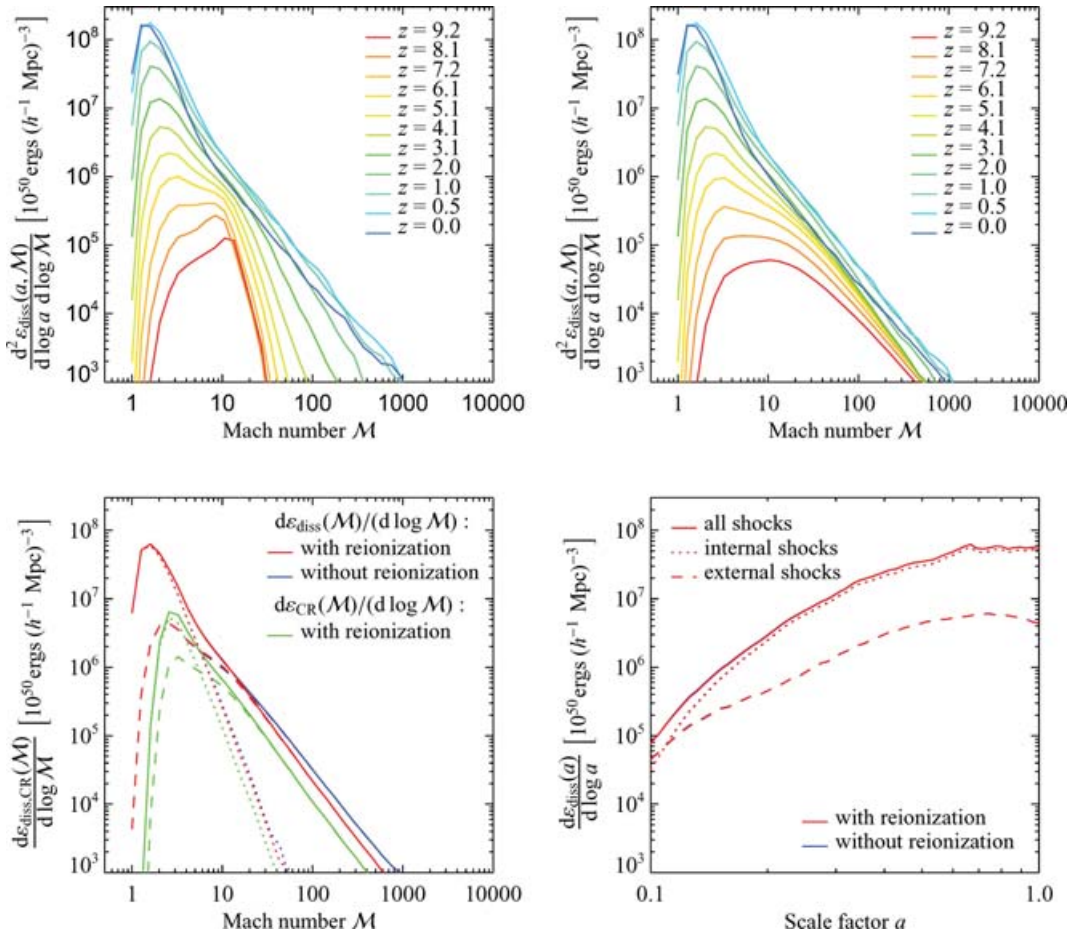

Figure 6. Influence of reionization on the Mach number statistics of non-radiative cosmological simulations. The top left-hand panel shows the differential Mach number distribution $d^2\varepsilon_{diss}(a, \mathcal{M})/(d\log a\, d\log\mathcal{M})$ for our reference simulation with reionization while the top right-hand panel shows this distribution for the simulation without reionization. The lower left-hand panel shows both distributions integrated over the scalefactor, $d\varepsilon_{diss}(\mathcal{M})/(d\log\mathcal{M})$ in addition to the Mach number distribution weighted by the injected CR energy rate normalized to the simulation volume, $d\varepsilon_{CR}(\mathcal{M})/(d\log\mathcal{M})$ (green). Internal shocks are shown with dotted lines and external shocks with dashed lines. The lower right-hand panel shows the evolution of the dissipated energy due to shock waves with scalefactor, $d\varepsilon_{diss}(a)/(d\log a)$. The models with and without reionization lie on top of each other.

deposition per particle of $E_{diss}\,\mu/(\rho_{crit}\Omega_b V) = 0.63\,\mathrm{keV}$, where $\mu = 4m_p/(3 + 5X_H)$ is the mean particle weight assuming full ionization and $X_H = 0.76$ is the primordial hydrogen mass fraction. Our results agree well with those of Ryu et al. (2003) in the case of internal shocks while our external shocks tend to be weaker. This can be attributed to our differing definition of internal/external shocks as we prefer a density criterion and use the critical pre-shock overdensity $\delta > 10$ for the classification of an internal shock.

6.3.2 Cosmic ray acceleration

In our non-radiative cosmological simulations we additionally calculate the expected shock-injected CR energy using our formalism of DSA described in Enßlin et al. (submitted). This formalism follows a model based on plasma physics for the leakage of thermal ions into the CR population. However, in the present analysis, the injected CR energy $du_{CR,inj}/(d\log a)$ was only monitored and not dynamically tracked. In our model, the CR population is described by single power-law distribution which is uniquely determined by the dimensionless momentum cut-off q, the normalization C, and the spectral index α. Considering shock-injected CRs only, the spectral index is determined by $\alpha = (x_s + 2)/(x_s - 1)$, where x_s denotes the density jump at the shock.

Our simplified model for the DSA fails in the limit of weak shocks and overpredicts the injection efficiency. Especially in this regime, Coulomb losses have to be taken into account which remove the low-energetic part of the injected CR spectrum efficiently on a short time-scale giving rise to an effective CR energy efficiency. Thus, the instantaneous injected CR energy $du_{CR,inj}/(d\log a)$ depends on the simulation time-step and the resolution. To provide a resolution-independent statement about the injected CR energy, we decided to rethermalize the injected CR energy below the cut-off $q_{threshold} = 0.83$. This cut-off has the desired property that it coincides with the kinematic threshold of the hadronic CR p–p interaction to produce pions which decay into secondary electrons (and neutrinos) and γ-rays:

$$\pi^{\pm} \rightarrow \mu^{\pm} + \nu_{\mu}/\bar{\nu}_{\mu} \rightarrow e^{\pm} + \nu_e/\bar{\nu}_e + \nu_{\mu} + \bar{\nu}_{\mu}$$
$$\pi^0 \rightarrow 2\gamma.$$

Only CR protons above this kinematic threshold are therefore visible through their decay products in both the γ-ray and radio bands via radiative processes, making them directly observationally detectable.

The lower left-hand panel of Fig. 6 shows the Mach number distribution weighted by the injected CR energy rate and normalized to the simulation volume, $\mathrm{d}\varepsilon_{\rm CR}(\mathcal{M})/(\mathrm{d}\log\mathcal{M})$ (solid green). The effect of the CR injection efficiency $\zeta_{\rm inj}=\varepsilon_{\rm CR}/\varepsilon_{\rm diss}$ can easily be seen: while the CR injection is saturated for strong shocks to $\zeta_{\rm max}=0.5$, in weak shocks most of the dissipated energy is thermalized and only small parts are used for the acceleration of relativistic particles. Effectively, this shifts the maximum and the mean value of the Mach number distribution weighted by the shock-dissipated energy towards higher values in the case of the distribution weighted by the injected CR energy. This effect is even stronger when considering only CRs with a lower cut-off $q=10,30$ which are responsible for radio haloes observed at frequencies above 100 MHz, assuming typical magnetic field strengths of $B=10,1\,\mu$G, respectively. This follows from the monoenergetic approximation of the hadronic electron production and synchrotron formula

$$\nu_{\rm s}=\frac{3eB}{2\pi m_{\rm e}c}\gamma_{\rm e}^2,\quad \text{where}\quad \gamma_{\rm e}\simeq\frac{q}{16}\frac{m_{\rm p}}{m_{\rm e}}, \tag{6.3}$$

where e denotes the elementary charge.

As the regime of strong shocks is dominated by external shocks where the CR injection is saturated, CRs are dynamically more important in dilute regions and dynamically less important at the cluster centres compared to the thermal non-relativistic gas. As weak shocks are mainly internal shocks we have to distinguish between their different appearance: strong internal shocks are most probably accretion shocks produced by infalling gas from sheets or filaments towards clusters, or peripheral merger shocks which steepen as they propagate outwards in the shallow cluster potential, highlighting the importance of CR injection in the outer cluster regions relative to thermally dissipated gas at shocks. In contrast, CR injection is dynamically less important in the case of flow shocks at the cluster centres or merging shock waves traversing the cluster centre. From these considerations we again draw the important conclusion that the ratio of CR-injected energy to dissipated thermal energy at shocks is an increasing function of decreasing density. Such a CR distribution is required within galaxy clusters to explain the diffuse radio synchrotron emission of galaxy clusters (so-called radio haloes) within the hadronic model of secondary electrons. For that, we assume a stationary CR electron spectrum which balances hadronic injection of secondaries and synchrotron and inverse Compton cooling processes (Brunetti 2002; Pfrommer & Enßlin 2004a,b). However, to make more precise statements about the origin of cluster radio haloes, more work is needed which studies the effect of the CR dynamics including CR diffusion and other CR-injection processes such as supernovae driven galactic winds.

6.3.3 Resolution study

To study numerical convergence we perform two additional simulations with a resolution of 2×128^3, respectively, for our models with and without reionization. Fig. 7 shows this resolution study for non-radiative cosmological simulations with a reionization epoch at $z=10$. The lower right-hand panel of Fig. 7 shows the evolution of the density-weighted temperature with redshift, $\langle(1+\delta)\,T\rangle_V(z)$. Shown are different resolutions in our models with and without reionization. The two differently resolved simulations (2×256^3 and 2×128^3) have converged well at redshifts $z\lesssim4$. In our reference simulation, the adiabatic decay of the mean temperature is halted at slightly higher redshift: because of the better mass resolution of this simulation, non-linear structures of smaller mass can be resolved earlier while converting part of their gravitational binding energy into internal energy through structure formation shock waves. In the simulation with reionization, the temperature increases discontinuously at $z=10$, declines again with the adiabatic expansion, until shock heating takes over at $z\sim7$–8 (depending on the resolution of the simulation). At $z=0$, all simulations yield a mean density-weighted temperature of $\simeq0.3$ keV. Comparing this density-weighted energy to the shock-deposited mean energy per particle of $E_{\rm diss}\simeq0.63$ keV, we obtain the mean adiabatic compression factor of the cosmic plasma, $\{kT/[(\gamma-1)\,E_{\rm diss}]\}^{1/(\gamma-1)}\simeq0.6$. After the plasma has been shock-heated, relaxation processes in the course of virialization let the plasma expand adiabatically on average. Secondly, mildly non-linear structures characterized by a shallow gravitational potential are partly effected by the Hubble flow which forces them to adiabatically expand.

The top left-hand panel shows the differential Mach number distribution $\mathrm{d}^2\varepsilon_{\rm diss}(a,\mathcal{M})/(\mathrm{d}\log a\,\mathrm{d}\log\mathcal{M})$ for our reference simulation with a resolution of 2×256^3 while the top right-hand panel shows this distribution for the simulation with a resolution of 2×128^3. The lower left-hand panel shows both distributions integrated over the scalefactor, $\mathrm{d}\varepsilon_{\rm diss}(\mathcal{M})/(\mathrm{d}\log\mathcal{M})$. Internal shocks are shown with dotted lines and external shocks with dashed lines. One immediately realizes that the question if the first shocks are fully converged among simulations of different resolution is not well posed because non-linear structures of smaller mass can be resolved collapsing earlier in higher-resolution simulations. Accordingly, the differential Mach number distribution is not well converged at redshifts $z\gtrsim6$ while the distribution is well converged for $z\lesssim3$. Since most of the energy is dissipated at late times, where our differential Mach number distribution is well converged, the integrated distribution, $\mathrm{d}\varepsilon_{\rm diss}(\mathcal{M})/(\mathrm{d}\log\mathcal{M})$, shows only marginal differences among the differently resolved simulations. In particular, our statements about CR injection at structure formation shocks are robust with respect to resolution issues.

7 SUMMARY AND CONCLUSIONS

We provide a formalism for identifying and estimating the strength of structure formation shocks in cosmological SPH simulations on-the-fly, both for non-relativistic thermal gas as well as for a plasma composed of a mixture of CRs and thermal gas. In addition, we derive an analytic solution to the one-dimensional Riemann shock-tube problem for the composite plasma of CRs and thermal gas (Appendix B). In the case of non-relativistic thermal gas, shock-tube simulations within a periodic three-dimensional box that is longer in x-direction than in the other two dimensions show that our formalism is able to unambiguously detect and accurately measure the Mach numbers of shocks, while in the case of plasma composed of CRs and thermal gas, the Mach numbers of shocks are estimated with an accuracy better than 10 per cent. In both cases, we find a very good agreement of the averaged simulated hydrodynamical quantities (such as density, pressure and velocity) and the analytic solutions. Using our formalism for DSA, we additionally calculate and monitor the shock-injected CR energy, but without dynamically tracking this CR energy component; the latter will be studied in forthcoming work. The good agreement between the simulated and theoretically expected shock-injected CR energy demonstrates that our formalism is reliably able to accelerate CRs instantaneously during the simulation.

Subsequently, we identified and studied structure formation shock waves using cosmological N-body/hydrodynamical SPH simulations for a concordance ΛCDM universe in a periodic cubic box of

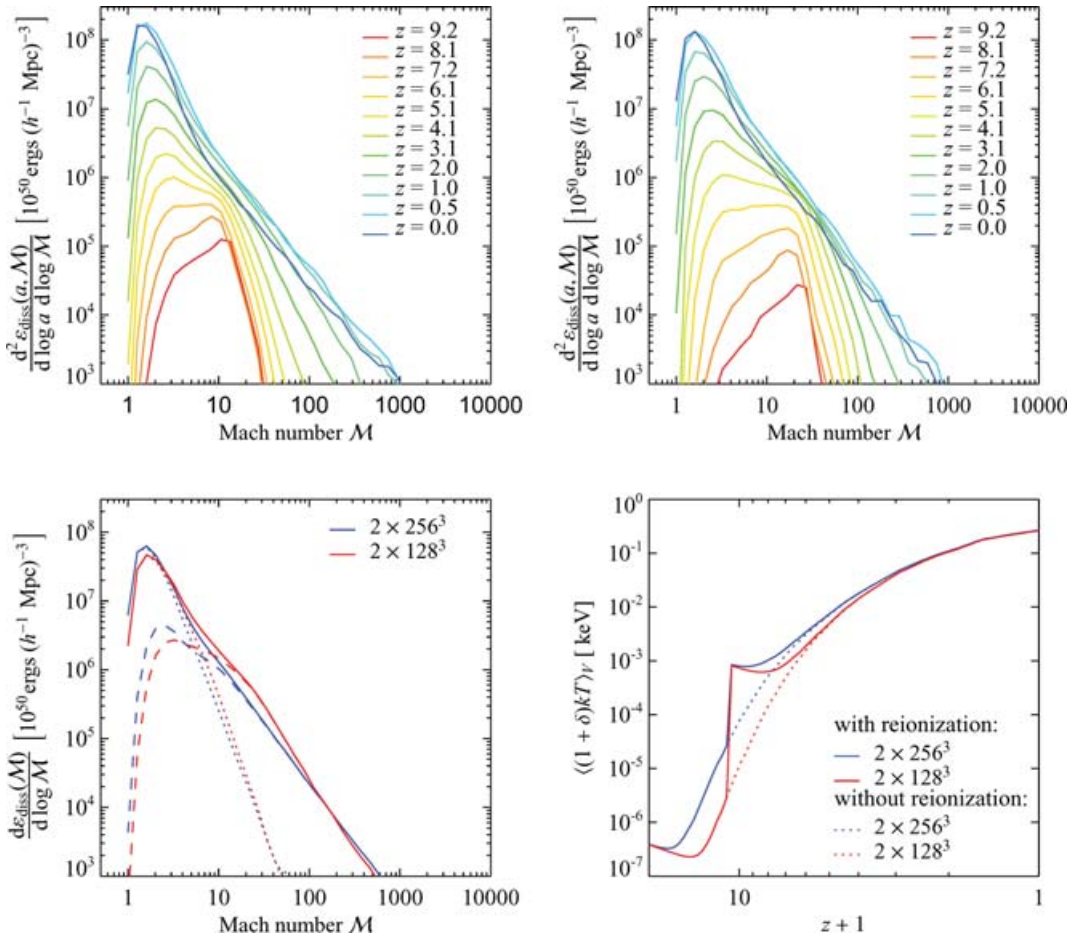

Figure 7. Resolution study: Mach number statistics for non-radiative cosmological simulations with a reionization epoch at $z = 10$. The top left-hand panel shows the differential Mach number distribution $d^2\varepsilon_{diss}(a, \mathcal{M})/(d\log a\, d\log\mathcal{M})$ for our reference simulation with a resolution of 2×256^3 while the top right-hand panel shows this distribution for the simulation with a resolution of 2×128^3. The lower left-hand panel shows both distributions integrated over the scalefactor, $d\varepsilon_{diss}(\mathcal{M})/(d\log\mathcal{M})$. Internal shocks are shown with dotted lines and external shocks with dashed lines. The lower right-hand panel shows the evolution of the density-weighted temperature with redshift. Shown are different resolutions in our models with and without reionization.

comoving size $100\,h^{-1}$ Mpc. We performed simulations with and without a reionization epoch at $z = 10$ in order to investigate the effects of reionization on the Mach number distribution. Our sets of simulations follow only non-radiative gas physics where we neglected additional physical processes, such as radiative cooling, star formation and feedback from galaxies and stars including CR pressure. Since we are mainly interested in shock waves situated mostly outside the cluster core regions, the conclusions drawn in this article should not be significantly weakened by the exclusion of those radiative processes. Furthermore, these simplifications align our work with the mesh-based simulations of Ryu et al. (2003) and enable a direct comparison and verification of our results. We classify cosmological shock waves as internal and external shocks, depending on whether or not the associated pre-shock gas was previously shocked (cf. Ryu et al. 2003). Rather than using a thermodynamical criterion such as the temperature, we prefer a density criterion such as the overdensity δ in order not to confuse the shock definition once we will follow radiatively cooling gas in galaxies. External shocks surround filaments, sheets and haloes where the pristine adiabatically cooling gas is shocked for the first time. Internal shocks on the other hand are located within the regions bound by external shocks and are created by flow motions accompanying hierarchical structure formation. Their population includes accretion shocks produced by infalling material along the filaments into clusters, merger shocks resulting from infalling haloes and flow shocks inside non-linear structures which are excited by supersonic motions of subclumps.

The Mach number distribution weighted by the dissipated energy shows in detail that most of the energy is dissipated in weak shocks which are situated in the internal regions of groups or clusters while collapsed cosmological structures are surrounded by external strong shocks which have a minor impact on the energy balance. The evolution of the Mach number distribution shows that the average shock strength becomes weaker at later times while there is an increasing amount of energy dissipated at shock waves as cosmic time evolves because the mean shock speed increases together with the characteristic mass of haloes forming during cosmic structure formation. For the same reason, internal shocks play a more important role than external shocks in dissipating energy associated with structure formation, especially at small redshift. The energy input through reionization processes influences the Mach number distribution primarily during a period following the reionization era and suppresses strong external shock waves efficiently because of the significant increase of the sound speed of the intergalactic medium.

Weighting the Mach number distribution by the injected CR energy shows the potential dynamical implications of CR populations in galaxy clusters and haloes: the maximum and the mean value of the Mach number distribution, weighted by the shock-dissipated energy, is effectively shifted towards higher values of the Mach number when the distribution is weighted by the injected CR energy. In other words, the average shock wave responsible for CR energy injection is stronger compared to the average shock which thermalizes the plasma. The fundamental reason for this lies in the theory of DSA at collisionless shock waves and can be phenomenologically described by a CR-injection efficiency: while the CR injection is saturated to an almost equipartition value between injected CR energy and dissipated thermal energy for strong shocks, in weak shocks most of the dissipated energy is thermalized and only small parts are used for the acceleration of relativistic particles. Relative to the thermal non-relativistic energy density, the shock-injected CR energy density is dynamically more important at the outer dilute cluster regions and less important at the cluster centres since weak shock waves predominantly occur in high-density regions. This has the crucial consequence that the ratio of CR injected energy to dissipated thermal energy is an increasing function as the density declines. Such a CR distribution within galaxy cluster is required to explain the diffuse radio synchrotron emission of galaxy clusters (so-called radio haloes) within the hadronic model of secondary electrons. In order to draw thorough conclusions about the origin of cluster radio haloes, more work is needed which studies the effect of the CR dynamics comprising of CR injection and cooling processes as well as CR diffusion mechanisms.

We note that our new formalism for shock detection in SPH simulations should have a range of interesting applications in simulations of galaxy formation. For example, when combined with radiative dissipation and star formation, our method can be used to study CR injection by supernova shocks, or to construct models for shock-induced star formation in the ISM (e.g. Barnes 2004). It should also be useful to improve the accuracy of predictions for the production of γ-rays by intergalactic shocks (e.g. Keshet et al. 2003).

ACKNOWLEDGMENTS

The authors would like to thank Ewald Müller, Björn Malte Schäfer and our referee Adrian Jenkins for carefully reading the manuscript and their constructive remarks.

REFERENCES

Abel T., Bryan G. L., Norman M. L., 2002, Sci, 295, 93
Barnes J. E., 2004, MNRAS, 350, 798
Berezhko E., Ksenofontov L., Yelshin V., 1995, Nucl. Phys. B Proc. Suppl., 39, A171
Berger M. J., Colella P., 1989, J. Comput. Phys., 82, 64
Berrington R. C., Dermer C. D., 2003, ApJ, 594, 709
Blandford R., Eichler D., 1987, Phys. Rep., 154, 1
Blasi P., Colafrancesco S., 1999, Astropart. Phys., 12, 169
Brunetti G., 2002, in Bowyer S., Hwang C.-Y., eds, ASP Conf. Ser., Matter and Energy in Clusters of Galaxies. Astron. Soc. Pac., San Francisco
Brunetti G., Setti G., Feretti L., Giovannini G., 2001, MNRAS, 320, 365
Brunetti G., Blasi P., Cassano R., Gabici S., 2004, MNRAS, 350, 1174
Bryan G. L., Norman M. L., 1997, in ASP Conf. Ser. Vol. 123, Computational Astrophysics; 12th Kingston Meeting on Theoretical Astrophysics. Astron. Soc. Pac., San Francisco, p. 363
Cen R., Ostriker J. P., 1993, ApJ, 417, 404
Cen R., Ostriker J. P., 1999, ApJ, 514, 1
Ciardi B., Stoehr F., White S. D. M., 2003, MNRAS, 343, 1101
Courant R., Friedrichs K. O., 1948, Supersonic Flow and Shock Waves. Pure and Applied Mathematics. Interscience, New York, 1948
Davé R. et al., 2001, ApJ, 552, 473
Deiss B. M., Reich W., Lesch H., Wielebinski R., 1997, A&A, 321, 55
Dennison B., 1980, ApJ, 239, L93
Dolag K., Enßlin T. A., 2000, A&A, 362, 151
Drury L. O., 1983, Rep. Prog. Phys., 46, 973
Ellison D. C., Baring M. G., Jones F. C., 1996, ApJ, 473, 1029
Enßlin T. A., Biermann P. L., Klein U., Kohle S., 1998, A&A, 332, 395
Evrard A. E., 1988, MNRAS, 235, 911
Furlanetto S. R., Loeb A., 2004, ApJ, 611, 642
Fusco-Femiano R., dal Fiume D., Feretti L., Giovannini G., Grandi P., Matt G., Molendi S., Santangelo A., 1999, ApJ, 513, L21
Gabici S., Blasi P., 2003, ApJ, 583, 695
Gingold R. A., Monaghan J. J., 1977, MNRAS, 181, 375
Giovannini G., Feretti L., Venturi T., Kim K. T., Kronberg P. P., 1993, ApJ, 406, 399
Hellsten U., Gnedin N. Y., Miralda-Escudé J., 1998, ApJ, 509, 56
Hernquist L., Katz N., 1989, ApJS, 70, 419
Jaffe W. J., 1977, ApJ, 212, 1
Jones T. W., Kang H., 2005, Astropart. Phys., 24, 75
Jubelgas M., Springel V., Enßlin T. A., Pfrommer C., MNRAS, submitted
Kang H., Jones T. W., 2005, ApJ, 620, 44
Kang H., Jones T. W., Gieseler U. D. J., 2002, ApJ, 579, 337
Kang H., Ryu D., Cen R., Song D., 2005, ApJ, 620, 21
Kennel C. F., Edmiston J. P., Hada T., 1985, Geophys. Union, Geophys. Monogr. Ser., 34, 1
Keshet U., Waxman E., Loeb A., Springel V., Hernquist L., 2003, ApJ, 585, 128
Kim K., Kronberg P. P., Giovannini G., Venturi T., 1989, Nat, 341, 720
Kravtsov A. V., Klypin A., Hoffman Y., 2002, ApJ, 571, 563
Kuo P., Bowyer S., Hwang C., 2005, ApJ, 618, 675
Loeb A., Waxman E., 2000, Nat, 405, 156
Lucy L. B., 1977, AJ, 82, 1013
Malkov M. A., 1998, Phys. Rev. E, 58, 4911
Malkov M. A., 1999, ApJ, 511, L53
Malkov M. A., O'C Drury L., 2001, Rep. Prog. Phys., 64, 429
Miniati F., 2002, MNRAS, 337, 199
Miniati F., Ryu D., Kang H., Jones T. W., Cen R., Ostriker J. P., 2000, ApJ, 542, 608
Miniati F., Jones T. W., Kang H., Ryu D., 2001, ApJ, 562, 233
Monaghan J. J., 1997, J. Comput. Phys., 136, 298
Monaghan J. J., Lattanzio J. C., 1985, A&A, 149, 135
Navarro J. F., White S. D. M., 1993, MNRAS, 265, 271
Norman M. L., Bryan G. L., 1999, in ASSL Vol. 240, Numerical Astrophysics. Kluwer, Boston, p. 19
Ohno H., Takizawa M., Shibata S., 2002, ApJ, 577, 658
Pavlidou V., Fields B. D., 2005, preprint (astro-ph/0504485)
Pen U., 1998, ApJS, 115, 19
Pfrommer C., Enßlin T. A., 2003, A&A, 407, L73
Pfrommer C., Enßlin T. A., 2004a, A&A, 413, 17
Pfrommer C., Enßlin T. A., 2004b, MNRAS, 352, 76
Quilis V., Ibanez J. M. A., Saez D., 1998, ApJ, 502, 518
Rasio F. A., Shapiro S. L., 1991, ApJ, 377, 559
Refregier A., Teyssier R., 2002, Phys. Rev. D, 66, 043002
Reimer O., Pohl M., Sreekumar P., Mattox J. R., 2003, ApJ, 588, 155
Röttgering H. J. A., Wieringa M. H., Hunstead R. W., Ekers R. D., 1997, MNRAS, 290, 577
Ryu D., Kang H., Hallman E., Jones T. W., 2003, ApJ, 593, 599
Sanders J. S., Fabian A. C., Dunn R. J. H., 2005, MNRAS, 360, 133
Sarazin C. L., 2002, in ASSL Vol. 272, Merging Processes in Galaxy Clusters: The Physics of Cluster Mergers. Kluwer, Dordrecht, p. 1
Schlickeiser R., Sievers A., Thiemann H., 1987, A&A, 182, 21
Sod G. A., 1978, J. Comput. Phys., 27, 1

Springel V., 2005, MNRAS, 364, 1105
Springel V., Hernquist L., 2002, MNRAS, 333, 649
Springel V., Yoshida N., White S. D. M., 2001, New Astron., 6, 79
Toro E. F., 1997, Riemann Solvers and Numerical Methods for Fluid Dynamics. Springer-Verlag, Berlin
Vestrand W. T., 1982, AJ, 87, 1266
Völk H. J., Aharonian F. A., Breitschwerdt D., 1996, Space Sci. Rev., 75, 279
Wentzel D. G., 1974, ARA&A, 12, 71
Yepes G., Kates R., Khokhlov A., Klypin A., 1995, in Maurogordato S., Balkowski C., Tao C., Van J. T. T., eds, Clustering in the Universe. Editions Frontiers, Paris, p. 209

APPENDIX A: RIEMANN SHOCK-TUBE PROBLEM

The Riemann shock-tube calculation of Sod (1978) has become a generally accepted test of numerical hydrodynamical codes. As a baseline for later extension, we present in the section the quasi-analytic solution for the Riemann problem in the standard case of a polytropic gas. Then, in Appendix B we derive the quasi-analytic solution in the case of a gas composed of CRs and thermal gas, where the effective adiabatic index depends on the different equations of state and changes across the shock tube.

In the following, we summarize the key considerations which lead to the solution of the Riemann problem, for completeness (see e.g. Courant & Friedrichs 1948; Toro 1997; Rasio & Shapiro 1991, for a compact representation). For the initial state, we assume a state with higher pressure in the left-half space without loss of generality. At any time $t>0$, this leads to the development of five regions of gas with different hydrodynamical states which are numbered in ascending order from the right-hand side. These regions are separated by the head and the tail of the leftwards propagating rarefaction wave, and the rightwards propagating contact discontinuity and the shock wave. Mass, momentum and energy-conservation laws are represented by the generalized Rankine–Hugoniot conditions for a given coordinate system:

$$\begin{aligned} \upsilon_{\rm d}[\rho] &= [\rho\upsilon], \\ \upsilon_{\rm d}[\rho\upsilon] &= [\rho\upsilon^2 + P], \\ \upsilon_{\rm d}\left[\rho\frac{\upsilon^2}{2} + \varepsilon\right] &= \left[\left(\rho\frac{\upsilon^2}{2} + \varepsilon + P\right)\upsilon\right]. \end{aligned} \tag{A1}$$

Here, $\upsilon_{\rm d}$ denotes the speed of the discontinuity under consideration with respect to our coordinate system and we introduced the abbreviation $[F] = F_i - F_j$ for the jump of some quantity F across the discontinuity. Within the leftwards propagating rarefaction wave, the generalized Riemann invariants yield an isentropic change of state, $\mathrm{d}s = 0$, and conserve the quantity Γ^+:

$$\Gamma^+ = \upsilon + \int_0^\rho \frac{c(\rho')}{\rho'}\mathrm{d}\rho' = \upsilon + \frac{2\,c(\rho)}{\gamma - 1} = \text{constant}. \tag{A2}$$

For the last step, we assumed a polytropic equation of state $P = A\rho^\gamma$. Appropriately combining these equations, the solution can be expressed as follows:

$$\rho(x,t) = \begin{cases} \rho_5, & x \leqslant -c_5 t, \\ \rho_5\left[-\mu^2\frac{x}{c_5 t} + (1-\mu^2)\right]^{2/(\gamma-1)}, & -c_5 t < x \leqslant -\upsilon_{\rm t} t, \\ \rho_3, & -\upsilon_{\rm t} t < x \leqslant \upsilon_2 t, \\ \rho_2, & \upsilon_2 t < x \leqslant \upsilon_{\rm s} t, \\ \rho_1, & x > \upsilon_{\rm s} t, \end{cases} \tag{A3}$$

$$P(x,t) = \begin{cases} P_5, & x \leqslant -c_5 t, \\ P_5\left[-\mu^2\frac{x}{c_5 t} + (1-\mu^2)\right]^{2\gamma/(\gamma-1)}, & -c_5 t < x \leqslant -\upsilon_{\rm t} t, \\ P_2 = P_3, & -\upsilon_{\rm t} t < x \leqslant \upsilon_{\rm s} t, \\ P_1, & x > \upsilon_{\rm s} t, \end{cases} \tag{A4}$$

$$\upsilon(x,t) = \begin{cases} 0, & x \leqslant -c_5 t, \\ (1-\mu^2)\left(\frac{x}{t} + c_5\right), & -c_5 t < x \leqslant -\upsilon_{\rm t} t, \\ \upsilon_2 = \upsilon_3, & -\upsilon_{\rm t} t < x \leqslant \upsilon_{\rm s} t, \\ 0, & x > \upsilon_{\rm s} t. \end{cases} \tag{A5}$$

Here, $\mu^2 = (\gamma-1)/(\gamma+1)$, $c_1 = \sqrt{\gamma P_1/\rho_1}$ and $c_5 = \sqrt{\gamma P_5/\rho_5}$ are the speeds of sound, $\upsilon_{\rm t}$ is the speed of propagation of the tail of the rarefaction wave, and $\upsilon_{\rm s}$ is the shock speed. The post-shock pressure is obtained by solving (numerically) the non-linear equation, which is derived from the Rankine–Hugoniot conditions over the shock while ensuring the conservation of the two Riemann invariants of equation (A2):

$$\left(\frac{P_2}{P_1} - 1\right)\sqrt{\frac{1-\mu^2}{\gamma\,(P_2/P_1 + \mu^2)}} - \frac{2}{(\gamma-1)}\frac{c_5}{c_1}\left[1 - \left(\frac{P_2}{P_5}\right)^{(\gamma-1)/(2\gamma)}\right] = 0. \tag{A6}$$

The density on the left-hand side of the contact discontinuity is $\rho_3 = \rho_5 (P_2/P_5)^{1/\gamma}$, since the gas is adiabatically connected to the left-hand side. The post-shock density ρ_2 is also derived from the Rankine–Hugoniot conditions,

$$\rho_2 = \rho_1 \left(\frac{P_2 + \mu^2 P_1}{P_1 + \mu^2 P_2} \right). \tag{A7}$$

The post-shock gas velocity υ_2 is obtained from the rarefaction wave equation, $x/t = \upsilon - c$, and usage of the Riemann invariant Γ^+:

$$\upsilon_2 = \upsilon_3 = \frac{2c_5}{(\gamma - 1)} \left[1 - \left(\frac{P_2}{P_5} \right)^{(\gamma-1)/(2\gamma)} \right], \tag{A8}$$

and from equation (A5) we derive the speed of propagation of the tail of the rarefaction wave $\upsilon_t = c_5 - \upsilon_2/(1-\mu^2)$. Finally, mass conservation across the shock yields

$$\upsilon_s = \frac{\upsilon_2}{1 - \rho_1/\rho_2}. \tag{A9}$$

APPENDIX B: RIEMANN SHOCK-TUBE PROBLEM FOR A COMPOSITE OF COSMIC RAYS AND THERMAL GAS

B1 Derivation

In contrast to the previous case, the composite of CRs and thermal gas does not obey a polytropic equation of state. In this section, we present an analytic derivation of the Riemann shock-tube problem for the composite of polytropic gas and a component that is adiabatically compressed at the shock such as relativistic gas or a homogeneous magnetic field which is parallel to the shock front. For the analytic derivation, we adopt the following two approximations: (i) we assume the CR adiabatic index (equation 2.6) to be constant over the shock tube and (ii) we neglect CR diffusion. The first assumption is justified as long as the CR pressure is not dominated by trans-relativistic CRs of low energy while the second assumption is a strong simplification with respect to simulating realistic shocks including CRs (Kang & Jones 2005). However, including CR diffusion complicates the problem significantly such that it is not any more analytically tractable.

For the initial state, we again assume a state with higher pressure in the left-half space. At any time $t > 0$, five regions of gas with different hydrodynamical states coexist, and are numbered in ascending order from the right-hand side. We use the notations $P_i = P_{\mathrm{CR},i} + P_{\mathrm{th},i}$ and $\varepsilon_i = \varepsilon_{\mathrm{CR},i} + \varepsilon_{\mathrm{th},i}$ for the composite quantities in region i. The full solution of the initial-value problem consists of determining 12 unknown quantities in the regions (2) and (3): $\rho_2, \upsilon_2, P_{\mathrm{CR2}}, P_{\mathrm{th2}}, \varepsilon_{\mathrm{CR2}}, \varepsilon_{\mathrm{th2}}$ and $\rho_3, \upsilon_3, P_{\mathrm{CR3}}, P_{\mathrm{th3}}, \varepsilon_{\mathrm{CR3}}, \varepsilon_{\mathrm{th3}}$. The thermal gas obeys a polytropic equation of state, i.e. $\varepsilon_{\mathrm{th},i} = P_{\mathrm{th},i}/(\gamma_{\mathrm{th}} - 1)$ for $i \in \{2, 3\}$ and the regions (2) and (3) are separated by a contact discontinuity, implying vanishing mass flux through it and thus, $\upsilon_2 = \upsilon_3$ and $P_2 = P_3$. This reduces the dimensionality of our problem to eight unknowns. In our approximation, the CRs are adiabatically expanded over the rarefaction wave and adiabatically compressed at the shock while obeying a polytropic equation of state:

$$\begin{aligned} P_{\mathrm{CR3}} &= P_{\mathrm{CR5}} \left(\frac{\rho_3}{\rho_5} \right)^{\gamma_{\mathrm{CR}}}, \quad \varepsilon_{\mathrm{CR3}} = \varepsilon_{\mathrm{CR5}} \left(\frac{\rho_3}{\rho_5} \right)^{\gamma_{\mathrm{CR}}}, \\ P_{\mathrm{CR2}} &= P_{\mathrm{CR1}} \left(\frac{\rho_2}{\rho_1} \right)^{\gamma_{\mathrm{CR}}}, \quad \varepsilon_{\mathrm{CR2}} = \varepsilon_{\mathrm{CR1}} \left(\frac{\rho_2}{\rho_1} \right)^{\gamma_{\mathrm{CR}}}, \end{aligned} \tag{B1}$$

which further reduces the dimensionality by four unknowns. Moreover, the thermal gas is also adiabatically expanded over the rarefaction wave yielding $P_{\mathrm{th3}} = P_{\mathrm{th5}} \, (\rho_3/\rho_5)^{\gamma_{\mathrm{th}}}$. Hence, we need three more linearly independent equations for the solution: two of them are obtained by considering the Rankine–Hugoniot conditions (equation A1) in a stationary system of reference with $\upsilon_{\mathrm{d}} = \upsilon_{\mathrm{s}}$. The last equation is given by the Riemann invariant Γ^+, where the effective speed of sound is given by $c = \sqrt{\gamma_{\mathrm{eff}} P/\rho}$:

$$\Gamma^+ = \upsilon + \int_0^\rho \frac{c(\rho')}{\rho'} \mathrm{d}\rho' = \upsilon + I(\rho) = \text{constant} \quad \text{with} \quad I(\rho) = \int_0^\rho \sqrt{\tilde{A}_{\mathrm{CR}} x^{\gamma_{\mathrm{CR}}-3} + \tilde{A}_{\mathrm{th}} x^{\gamma_{\mathrm{th}}-3}} \, \mathrm{d}x. \tag{B2}$$

Here, we use the abbreviations $\tilde{A}_i = \gamma_i A_i$ where $i \in \{\mathrm{th}, \mathrm{CR}\}$ and $A_i = P_i \, \rho^{-\gamma_i}$ denotes the invariant adiabatic function over the rarefaction wave. Introducing the difference of the adiabatic indices of the two populations, $\Delta\gamma = \gamma_{\mathrm{th}} - \gamma_{\mathrm{CR}}$, the solution to the integral $I(\rho)$ is given by

$$I(\rho) = \frac{\sqrt{\tilde{A}_{\mathrm{CR}}}}{\Delta\gamma} \left(\frac{\tilde{A}_{\mathrm{CR}}}{\tilde{A}_{\mathrm{th}}} \right)^{(\gamma_{\mathrm{CR}}-1)/(2\Delta\gamma)} \mathcal{B}_{x(\rho)} \left(\frac{\gamma_{\mathrm{CR}} - 1}{2\Delta\gamma}, \frac{1 - \gamma_{\mathrm{th}}}{2\Delta\gamma} \right) \quad \text{with} \quad x(\rho) = \frac{\tilde{A}_{\mathrm{th}} \, \rho^{\gamma_{\mathrm{th}}}}{\tilde{A}_{\mathrm{CR}} \, \rho^{\gamma_{\mathrm{CR}}} + \tilde{A}_{\mathrm{th}} \, \rho^{\gamma_{\mathrm{th}}}}. \tag{B3}$$

Although the second argument of the incomplete Beta function is always negative, $I(\rho)$ is well defined as long as we consider a non-zero CR pressure which is characterized by $\tilde{A}_{\mathrm{CR}} > 0$ and γ_{CR} sufficiently far from γ_{th}, i.e. $\Delta\gamma > 0$. For $\tilde{A}_{\mathrm{CR}} = 0$, the integral can be solved in closed form, yielding $I(\rho) = 2c(\rho)/(\gamma_{\mathrm{th}} - 1)$.

B2 Solution of the Riemann problem

The densities leftwards and rightwards of the contact discontinuity, ρ_3 and ρ_2, are obtained by solving (numerically) the following non-linear system of equations. It is derived from matching the possible post-shock states (pressure and density) with the possible post-rarefaction wave

states while simultaneously ensuring the conservation laws over the rarefaction wave and the shock:

$$\begin{aligned} f_1(x_\mathrm{s}, x_\mathrm{r}) &\equiv [P_2(x_\mathrm{r}) - P_1]\,(x_\mathrm{s} - 1) - \rho_1 x_\mathrm{s}\,[I(\rho_5) - I(x_\mathrm{r}\rho_5)]^2 = 0, \\ f_2(x_\mathrm{s}, x_\mathrm{r}) &\equiv [P_2(x_\mathrm{r}) + P_1]\,(x_\mathrm{s} - 1) + 2[x_\mathrm{s}\varepsilon_1 - \varepsilon_2(x_\mathrm{s}, x_\mathrm{r})] \quad = 0. \end{aligned} \tag{B4}$$

Here, we introduced the shock compression ratio $x_\mathrm{s} \equiv \rho_2/\rho_1$ and the rarefaction ratio $x_\mathrm{r} \equiv \rho_3/\rho_5$. Furthermore, the implicit dependences on x_s and x_r can explicitly be expressed as follows:

$$P_2(x_\mathrm{r}) = P_3(x_\mathrm{r}) = P_{\mathrm{CR}5} x_\mathrm{r}^{\gamma_\mathrm{CR}} + P_{\mathrm{th}5} x_\mathrm{r}^{\gamma_\mathrm{th}}, \tag{B5}$$

$$P_{\mathrm{CR}2}(x_\mathrm{s}) = P_{\mathrm{CR}1} x_\mathrm{s}^{\gamma_\mathrm{CR}}, \tag{B6}$$

$$\varepsilon_2(x_\mathrm{s}, x_\mathrm{r}) = \varepsilon_{\mathrm{CR}1} x_\mathrm{s}^{\gamma_\mathrm{CR}} + \frac{1}{\gamma_\mathrm{th} - 1}[P_2(x_\mathrm{r}) - P_{\mathrm{CR}2}(x_\mathrm{s})]. \tag{B7}$$

The roots of the non-linear system of equations (equation B4) immediately yield the post-shock pressure of the fluid via equation (B5). The post-shock velocity $\upsilon_2 = \upsilon_3$ and the shock speed υ_s are then obtained from the Rankine–Hugoniot relations,

$$\upsilon_2 = \sqrt{[P_2(x_\mathrm{r}) - P_1]\,\frac{\rho_2 - \rho_1}{\rho_2 \rho_1}}, \tag{B8}$$

$$\upsilon_\mathrm{s} = \frac{\rho_2 \upsilon_2}{\rho_2 - \rho_1}. \tag{B9}$$

Using the previous results, we can construct the solution to the generalized Riemann problem for CRs and thermal gas as follows:

$$\rho(x,t) = \begin{cases} \rho_5, & x \leqslant -c_5 t, \\ \rho(x,t), & -c_5 t < x \leqslant -\upsilon_\mathrm{t} t, \\ \rho_3, & -\upsilon_\mathrm{t} t < x \leqslant \upsilon_2 t, \\ \rho_2, & \upsilon_2 t < x \leqslant \upsilon_\mathrm{s} t, \\ \rho_1, & x > \upsilon_\mathrm{s} t, \end{cases} \tag{B10}$$

$$P(x,t) = \begin{cases} P_5, & x \leqslant -c_5 t, \\ A_\mathrm{CR}\,\rho(x,t)^{\gamma_\mathrm{CR}} + A_\mathrm{th}\,\rho(x,t)^{\gamma_\mathrm{th}}, & -c_5 t < x \leqslant -\upsilon_\mathrm{t} t, \\ P_2 = P_3, & -\upsilon_\mathrm{t} t < x \leqslant \upsilon_\mathrm{s} t, \\ P_1, & x > \upsilon_\mathrm{s} t, \end{cases} \tag{B11}$$

$$\upsilon(x,t) = \begin{cases} 0, & x \leqslant -c_5 t, \\ \frac{x}{t} + \sqrt{\tilde{A}_\mathrm{CR}\,\rho(x,t)^{\gamma_\mathrm{CR}-1} + \tilde{A}_\mathrm{th}\,\rho(x,t)^{\gamma_\mathrm{th}-1}}, & -c_5 t < x \leqslant -\upsilon_\mathrm{t} t, \\ \upsilon_2 = \upsilon_3, & -\upsilon_\mathrm{t} t < x \leqslant \upsilon_\mathrm{s} t, \\ 0, & x > \upsilon_\mathrm{s} t. \end{cases} \tag{B12}$$

Here, $c_5 = \sqrt{\gamma_{\mathrm{eff}5} P_5/\rho_5}$ is the effective speed of sound, υ_t is the speed of propagation of the tail of the rarefaction wave and υ_s is the shock speed. Matching the rarefaction wave equation to the density of the post-contact discontinuity yields υ_t:

$$\upsilon_\mathrm{t} = I(\rho_3) - I(\rho_5) + \sqrt{\tilde{A}_\mathrm{CR}\,\rho_3^{\gamma_\mathrm{CR}-1} + \tilde{A}_\mathrm{th}\,\rho_3^{\gamma_\mathrm{th}-1}}. \tag{B13}$$

The density within the rarefaction regime is obtained by solving (numerically) the non-linear equation for a given (x, t), which is derived from the rarefaction wave equation,

$$I[\rho(x,t)] - I(\rho_5) + \frac{x}{t} + \sqrt{\tilde{A}_\mathrm{CR}\,\rho(x,t)^{\gamma_\mathrm{CR}-1} + \tilde{A}_\mathrm{th}\,\rho(x,t)^{\gamma_\mathrm{th}-1}} = 0. \tag{B14}$$

This paper has been typeset from a TEX/LATEX file prepared by the author.